

Topological Properties of Bilayer α - T_3 Lattice Induced by Polarized Light

O. Benhaida,^{1,2} E. H. Saidi,^{1,2,3} L. B. Drissi,^{1,2,3,*} and R. Ahl Laamara^{1,2}

¹*LPHE, Modeling and Simulations, Faculty of Science,
Mohammed V University in Rabat, Rabat, Morocco*

²*CPM, Centre of Physics and Mathematics, Faculty of Science,
Mohammed V University in Rabat, Rabat, Morocco*

³*College of Physical and Chemical Sciences, Hassan II Academy of Sciences and Technology, Rabat, Morocco*

We investigate the topological properties of photon-dressed energy bands in bilayer α - T_3 lattices under off-resonant circularly polarized light, focusing on aligned and cyclic stacking configurations. Analytical expressions for quasi-energy bands are derived for aligned stacking, while numerical results address cyclic stacking at Dirac points. Circularly polarized light breaks the time-reversal symmetry, lifting the degeneracies at the intersections $t^{a,c}$, leading to the appearance of a Haldane-type Chern insulator in the absence of a magnetic field. At $\alpha = 1/\sqrt{2}$, orbital magnetic moments of corrugated and flat bands exhibit opposite signs, as do their Berry curvatures. For $0 < \alpha < 1$, light-induced band deformations near Dirac points create gaps in the quasi-energy spectrum, where the chemical potential modulates orbital magnetization. Linear magnetization variations align with Chern numbers, yielding quantized anomalous Hall conductivity across stacking types. Notable particle-hole symmetry breaking within $0 < \alpha < 1$ suggests applications in valley caloritronics and quantum sensing. At $\alpha = 1$, flat and corrugated bands remain undistorted; while the flat band contributes no Berry curvature, it produces a finite negative orbital magnetic moment, contrasting with the positive moment of the corrugated band.

KEYWORDS: topological properties; bilayer α - T_3 ; flat bands; off-resonant circularly polarized light; Berry curvature.

I. INTRODUCTION

Topological phases of matter have garnered significant interest revealing a rich tapestry of phenomena that challenge our understanding of condensed matter systems [1]-[4]. The interplay between topology and symmetry leads to exotic states, such as quantum Hall insulators and topological insulators, where edge states are robust against disorder [5-7]. These edge states are protected by the topological invariants that characterize the bulk properties of the material, making them resilient to perturbations that would typically localize or scatter electronic states [8, 9]. In addition to these well-known phases, Weyl semimetals have emerged as a new class of materials exhibiting unique features such as Fermi arcs on their surfaces [10]. Higher-order topological insulators further enrich this landscape by exhibiting boundary modes localized at corners or hinges, providing a new dimension to the study of topological phenomena [11-13]. Furthermore, the discovery of Majorana bound states in topological superconductors has opened pathways for fault-tolerant quantum computing, as these states can encode quantum information in a non-local manner [14, 15].

Periodically driven electronic and photonic systems have seen remarkable advancements in recent years, leading to the discovery of new phenomena and applications across various fields. The non-equilibrium dynamics underlying these systems, as described by Floquet theory [16, 17], have emerged as a powerful tool for investigating non-trivial topological phases in two-dimensional materials [18-22]. Applying Floquet engineering to photonic crystals allows the observation of the anomalous quantum Hall effect by imaging topological edge states that arise from periodic driving [23]. Thermalization processes under periodic driving lead to unique dynamics that differ from equilibrium systems [24]. Unconventional superconductivity in twisted bilayer graphene (TBG) at a magic angle [25] and in TBG aligned with boron nitride, demonstrating isolated flat bands under external electric fields [26, 27] complemented this landscape with respect to Conventional 2D superconductors [28]. These findings not only enhance our understanding of topological phases but also pave the way for innovative applications in quantum technologies and materials science.

Interestingly, the light-induced Hall effect in graphene has stimulated extensive research into Floquet topological phases [29]. This area of study encompasses a variety of phenomena, including topological phase transitions and the emergence of Floquet spin states [30]. These investigations have revealed a range of exotic behaviors that challenge conventional understandings of quantum materials [31, 32]. A crucial mechanism underlying these effects is the modification of the band structure through virtual photon processes, which occur under off-resonant circularly polarized

* Corresponding author: ldrissi@fsr.ac.ma

light irradiation. This is also exemplified by the emergence of flat bands in systems such as Kagome [33], T_3 or Dice [34], and Lieb lattices [35]. Of particular note is the fact that the T_3 or Dice lattice exhibits flat bands in the vicinity of charge neutrality, which results in electronic bands devoid of dispersion [36, 37]. The dice lattice structure can be realized through various experimental techniques. Traditionally, it has been constructed by epitaxially growing three layers of cubic lattices, such as $SrTiO_3/SrIrO_3/SrTiO_3$, along the (111) crystallographic direction [38].

Alternatively, optical lattice techniques have been proposed, where the interference of three pairs of counter-propagating laser beams at a wavelength of $\lambda = 3a/2$ (a being the lattice constant) can generate the dice lattice geometry. Theoretical proposals have been made to realize the $\alpha - T_3$ optical lattice, for example, by introducing a phase difference between one of the laser pairs [39, 40]. This approach offers a degree of tunability as the parameter α , which controls the lattice geometry, can be continuously modified by adjusting the laser phase. Furthermore, the low-energy behavior of certain quantum well systems, such as $Hg_1 - xCd_xTe$, can be effectively mapped onto the $\alpha - T_3$ model for appropriate doping levels, with α taking the specific value of $1/\sqrt{3}$ [41]. The $\alpha - T_3$ lattice has attracted significant research interest due to its tunable band structure and potential for realizing novel topological states [42–44]. A key feature of the $\alpha - T_3$ model is the continuously varying Berry phase from π (graphene) to 0 (dice lattice) as the parameter α is adjusted [45]. This unique characteristic allows for the study of how the Berry phase influences various physical phenomena. Several studies have explored the dependence of transport and optical properties on the Berry phase in the $\alpha - T_3$ lattice. The impact of α on the quantum Hall conductivity, dynamic longitudinal photoconductivity, and SdH oscillations was demonstrated in [45]. Additionally, the effect of varying Berry phase on orbital magnetostriction has been observed [40]. Transport measurements by Biswas and al. [42] revealed a smooth transition in the Hall conductivity from $\sigma_{xy} = 2(2n + 1)(e^2/h)$ to $\sigma_{xy} = 4n(e^2/h)$ with increasing α (n being an integer), highlighting the interplay between the model parameter and the topological behavior. Studies have explored the interplay between Floquet states and the Berry phase in the $\alpha - T_3$ lattice irradiated with circularly polarized resonant light [46]. This work highlighted the crucial role of resonance in inducing a Berry phase-dependent optical gap. Conversely, off-resonant circularly polarized radiation has been demonstrated to open gaps in various material systems, including graphene [47], topological insulator surface states [47], silicene [48], quasi-Dirac systems [49] and MoS2 [50]. This process transforms these materials into Chern insulating states. It is important to note that, as emphasized by Kitagawa et al. [20], the multiple Floquet bands formed by resonant light cannot be directly treated as a new, static band structure for calculating transport properties in these non-equilibrium systems. Notably, even higher Chern numbers were observed in single-layer Dice lattices [51]. A Haldane-like model on a Dice lattice predicted Chern numbers of ± 2 for the dispersive valence and conduction bands and 0 for the flat middle band. Additionally, this system exhibited a quantum anomalous Hall effect with two chiral edge channels [51]. The $\alpha - T_3$ lattice exhibits a unique behavior near charge neutrality. While the flat bands become dispersed when touching high-symmetry points (K and K' in the presence of spin-orbit coupling, they retain their non-trivial character [52]. Recent work by Tamang et al. [53] explored the topological properties of the $\alpha - T_3$ lattice using off-resonant circularly polarized light and found that the Berry curvature and orbital magnetic moment associated with the flat band change signs at $\alpha = 1/\sqrt{2}$. Moreover, the slopes of the linear regions of the orbital magnetization were shown to be closely related to the Chern numbers on either side of this critical α value. When two layers of the $\alpha - T_3$ lattice are stacked on top of each other to form a bilayer lattice with unequal stacking, the low-energy effective model exhibits a dispersive nature of the flat bands near the charge neutrality point [54]. The effect of Haldane flow on this lattice has also been analyzed, as it separates the six bands and determines non-zero Chern numbers for each band, giving the system distinctive topological properties. Furthermore, continuous modification of the scaling parameter α leads to topological phase transitions that occur through the band crossings, causing discontinuous changes in the Chern numbers of the lower conduction and valence bands, where these changes depend on the next-nearest-neighbor jump strength and appear at specific values of the scaling parameter α [55]. To date, no studies have investigated the topological signatures of bilayer $\alpha - T_3$ lattices under irradiation.

This study investigates emerging topological features in the $\alpha - T_3$ bilayer for aligned and cyclic stacks subjected to circularly polarized light in the off-resonance regime. This irradiation induces an effective mass term in the Hamiltonian, which breaks the time-reversal symmetry and transforms the semi-metallic behaviour of these stacks into a Haldane-type Chern insulator near Dirac points. To analyze these topological transitions, we propose to calculate Berry curvature, orbital magnetic moment, orbital magnetization, and anomalous Hall conductivity. These physical quantities are sensitive indicators of the system's topology. For example, the Berry curvature associated with corrugated and flat bands changes sign when the control parameter α is varied around the critical value $1/\sqrt{2}$. The orbital magnetic moment shows a similar inversion at this same value of α , clearly indicating the existence of a topological phase transition. In the presence of gaps, the orbital magnetization exhibits linear behaviour, which is a topological signature. These linear regions correlate with Chern numbers. Furthermore, the anomalous Hall conductivity also adopts a topological behaviour when the chemical potential within the gaps varies, leading to the appearance of plateaus. These plateaus appear when the parameters α and light amplitude (the latter being proportional to the mass term) are controlled and are also observed in the Haldane model applied to cyclic stacking, as proposed by P. Parui [55].

By modulating the electron-photon coupling, it is possible to realize the Haldane model in an $\alpha - T_3$ bilayer. The broken particle-hole symmetry, observed through properties, leads to valley anomalies for $0 < \alpha < 1$. In addition, the behaviour of the polarized valley current has also been studied under the effect of circularly polarized light irradiating a monolayer $\alpha - T_3$ lattice, with the aim of investigating the topological properties of this current [53, 56]. These results are promising and could pave the way for future applications in valley caloritronics and quantum sensing.

This paper is organized as follows: In Section II, we present a Hamiltonian model for the bilayer system in both aligned and cyclic stacks and outline the method for extracting the effective Hamiltonian induced by circularly polarized light, focusing on time-reversal and particle-hole symmetries. In Section II, the results from Section II A are discussed in the context of quasi-energy. Sections II B, II C and II D explore topological features, including Berry curvature, the orbital magnetic moment, and orbital magnetization. Additionally, Section II E provides an analysis of the anomalous Hall conductivity. Finally, the paper concludes with a comprehensive summary of the results presented in Section III.

II. THEORETICAL MODEL

This section aims to construct the Hamiltonian describing the electronic properties of $\alpha - T_3$ bilayers. We restrict our attention to aligned and cyclic stacking configurations. Prior to detailing the $\alpha - T_3$ bilayer, we examine the $\alpha - T_3$ monolayer, an extension of the honeycomb lattice. This lattice comprises two sublattices (A and B) augmented by additional sites (sublattice C) at the center of each hexagonal unit cell. Within this lattice, a quasiparticle can transition between C sites and alternate sites (e.g., B). Atoms within the A and C sublattices occupy edge positions, each connected to three neighbouring atoms. In contrast, B sites adopt a central hub configuration with six neighbouring connections. The hopping amplitude between A and B sites is given by $\cos \phi$, while that between B and C sites is $\sin \phi$, where ϕ dictates the hopping amplitude. This angle ϕ is related to another parameter α via the relation $\alpha = \tan \phi$. The real parameter α serves as an interpolation between the limiting cases of the model: the graphene lattice ($\alpha = 0$) and the cubic lattice ($\alpha = 1$). The lattice is defined as an $\alpha - T_3$ lattice for intermediate values of α in the range $0 < \alpha < 1$.

In an $\alpha - T_3$ bilayer system, the $\alpha - T_3$ bilayer consists of four vertically aligned, incommensurate stacking configurations [57]. For the purpose of this study, we will focus on only two of these stacking arrangements. There are multiple ways to stack two proportional $\alpha - T_3$ lattices with vertically aligned sites. The simplest configuration involves aligning corresponding sublattices in both layers: (A_u, B_u, C_u) in the top layer directly above (A_l, B_l, C_l) in the bottom layer, termed 'aligned' stacking $(A_l A_u - B_l B_u - C_l C_u)$, as shown in Figure 1(iv). A 'cyclic' stacking arrangement can be derived by displacing one layer of the aligned stack by a distance a , the lattice constant. This shift aligns sublattices A_l , B_l , and C_l from one layer with C_u , A_u , and B_u , respectively, in the other layer, resulting in a periodic sublattice arrangement $(A_l B_u - B_l C_u - C_l A_u)$ see Figure 1(v).

Within the $\alpha - T_3$ bilayer system there are two distinct, vertically aligned and non-equivalent stacking configurations: $A_l A_u - B_l B_u - C_l C_u$ (aligned) and $A_l B_u - B_l C_u - C_l A_u$ (cyclic). The interlayer hopping within these stacks is modelled by means of a tight-binding Hamiltonian [58], which includes the corresponding states of the sub-lattices A_u , C_u , B_u , A_l , B_l and C_l .

$$\mathcal{H}^\xi(\mathbf{q}, t_\perp^a, t_\perp^c) = \begin{pmatrix} 0 & \sin \phi f_{\mathbf{q}}^\xi & 0 & t_\perp^a & 0 & t_\perp^c \\ \sin \phi f_{\mathbf{q}}^{\xi*} & 0 & \cos \phi f^\xi(q) & t_\perp^c & t_\perp^a & 0 \\ 0 & \cos \phi f_{\mathbf{q}}^{\xi*} & 0 & 0 & t_\perp^c & t_\perp^a \\ t_\perp^a & t_\perp^c & 0 & 0 & \sin \phi f_{\mathbf{q}}^\xi & 0 \\ 0 & t_\perp^a & t_\perp^c & \sin \phi f_{\mathbf{q}}^{\xi*} & 0 & \cos \phi f_{\mathbf{q}}^\xi \\ t_\perp^c & 0 & t_\perp^a & 0 & \cos \phi f_{\mathbf{q}}^{\xi*} & 0 \end{pmatrix} \quad (1)$$

The Hamiltonian $\mathcal{H}^\xi(\mathbf{q}, t_\perp^a, 0)$ and $\mathcal{H}^\xi(\mathbf{q}, 0, t_\perp^c)$ describe the electronic properties of the aligned and cyclic $\alpha - T_3$ bilayer lattice, respectively. Here, $\mathbf{q} = (q_x, q_y)$ is the wavevector in the Brillouin zone, and $f(q) = \sum_{j=1}^3 e^{-i\mathbf{q}\delta_j}$, where the vectors δ_1 , δ_2 and δ_3 define the relative positions of the A sites with respect to their three nearest C neighbors. The vectors $-\delta_1$, $-\delta_2$ and $-\delta_3$ correspond to the relative positions of the A sites with respect to their three nearest B neighbors. The terms t represent the nearest-neighbor hopping amplitudes. Explicitly, the vectors δ_j are given by: $\delta_1 = a(0, 1)$, $\delta_2 = a(\sqrt{3}, -1)/2$, $\delta_3 = a(-\sqrt{3}, -1)/2$, where a is the distance between a site and its nearest neighbors, and t_\perp^a and t_\perp^c represent the interlayer coupling amplitudes for aligned and cyclic stacking, respectively. The energy spectrum of the system, calculated over the entire Brillouin zone, exhibits six bands. For an aligned stacking, two bands $\varepsilon_{2,5} = \pm t_\perp$ are flat while the remaining four $\varepsilon_{1,3,4,6} = \pm t_\perp + \mp |f(q)|$ exhibit dispersion and electron-hole symmetry. This spectrum is independent of the parameter α and is similar to that of a bilayer graphene

A-A stacking. Figure 1(i) illustrates this band structure, showing two shifted replicas of the single-layer $\alpha - T_3$ band structure, with gapless band crossings at the K (K') points. For a cyclic stacking, we have numerically calculated the eigenvalues of the tight-binding Hamiltonian. Figure 1(ii) presents the energy spectrum in the vicinity of the K(K') points. We observe four dispersive bands and two flat bands that become corrugated due to interlayer coupling. This spectrum exhibits a dependence on the parameter α , which we have fixed at a value of 1 in this study. At the band crossings at the K(K') points, we note the absence of an energy gap.

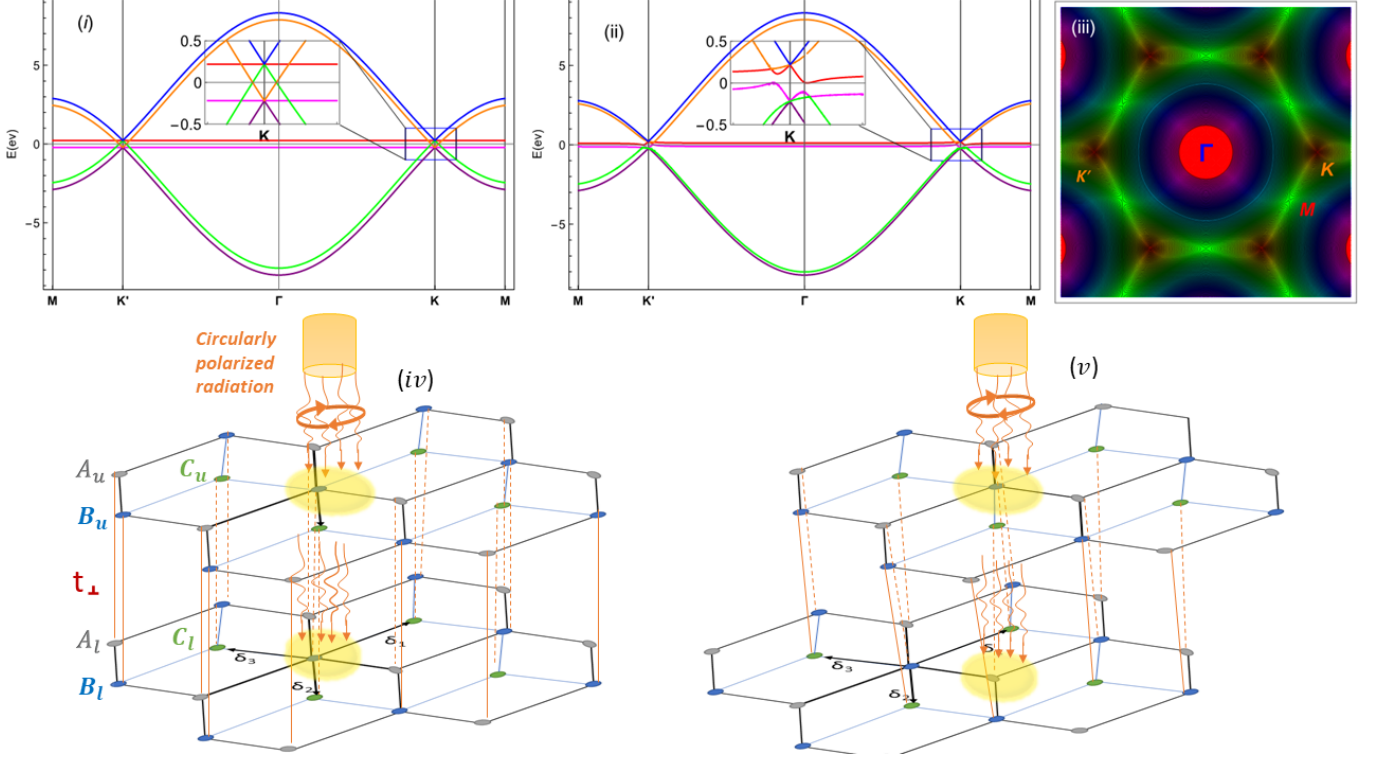


FIG. 1. We present the band structures of the $\alpha - T_3$ bilayer lattice for two types of stacking: (i) aligned stacking ($A_1A_u - B_1B_u - C_1C_u$) and (ii) cyclic stacking ($A_1B_u - B_1C_u - C_1A_u$). The graph illustrates the calculated bands along the qx axis at the high-symmetry points ($M - K' - \Gamma - K - M$) in the Brillouin zone, as shown in Figure (iii). For the nearest-neighbor hopping, a parameter value of $t = 2.7$ eV and interlayer coupling $t_\perp = t_\perp^a = t_\perp^c = 0.22$ eV are considered, assuming these values are analogous to those of graphene[85] and (iv) a Schematic diagram of the aligned stacked bilayer exposed to off-resonance circular polarization, and (v) a schematic diagram of the cyclic stacked bilayer.

In the low energy regime, where $|f(k)| \ll t_c$, quasiparticles exhibit semi-metallic behaviour. The electron and hole bands occupy different of the Brillouin zone, as shown in Figure 1. In the low-energy regime near the band crossing point t_c of the Dirac cone K(K'), the system behaves as a semimetal in the absence of external fields. Introducing a Haldane gap at the Dirac points, particularly at the crossing points t_c , through external perturbations, drives the system into a topological insulator phase. Furthermore, we demonstrate that off-resonant circularly polarized light irradiation induces gap openings, leading to the formation of topological states and the emergence of characteristic topological signatures in the bilayer $\alpha - T_3$ lattice.

In the low energy limit, a Taylor expansion of $f(q)$ around the Dirac point K in the Brillouin zone yields the approximation $f(k) \approx \hbar v_f (\xi k_x - i k_y)$. Here $k = q - K_\xi$ represents the wave vector measured relative to the points $K(\xi = +1)$ and $K'(\xi = -1)$ located at $\mathbf{K}_\xi = \xi 4\pi / (3\sqrt{3}a) \{1, 0\}$. where $v_F = 3\gamma_0 a / (2\hbar)$ is the Fermi velocity and $\xi = \pm$ is the valley index.

We consider an $\alpha - T_3$ bilayer lattice being irradiated with circularly polarized radiation perpendicular to the lattice plane, as depicted in Figure 1(iv)-(v). The associated vector potential is $\mathbf{A}(t) = A_0 (\cos \omega t, \sin \omega t)$, with $A_0 = E_0 / \omega$ and ω representing the electric field's amplitude and the radiation's frequency, respectively. Pierl's substitution of $\mathbf{k} \rightarrow \mathbf{k} + e\mathbf{A}(t)/\hbar$ in equation (1) leads to a modification of the Hamiltonian due to the minimal coupling between the external radiation and the system.

$$\mathcal{H}^\xi(\mathbf{k}, t_\perp^a, t_\perp^c, t) = \mathcal{H}^\xi(\mathbf{k}, t_\perp^a, t_\perp^c) + \xi c_0 P_- e^{i\xi\omega t} + \xi c_0 P_+ e^{-i\xi\omega t}. \quad (2)$$

where c_0 is the interaction coefficient, which is equal to $v_F e A_0$, $P_- = \mathbb{1}_{2 \times 2} \otimes \sigma_-$ and P_+ is the conjugate of P_- , we define σ_- as follows:

$$\sigma_- = \begin{pmatrix} 0 & 0 & 0 \\ \sin \phi & 0 & 0 \\ 0 & \cos \phi & 0 \end{pmatrix}. \quad (3)$$

Thus the wave functions for Dirac electrons obey the time-dependent Schrödinger equation.

$$\mathcal{H}^\xi(\mathbf{k}, t_\perp^a, t_\perp^c, t) |\psi(t)\rangle = i\hbar \partial_t |\psi(t)\rangle. \quad (4)$$

The Hamiltonian we are currently working on is periodic $\mathcal{H}^\xi(\mathbf{k}, t_\perp^a, t_\perp^c, t + T) = \mathcal{H}^\xi(\mathbf{k}, t_\perp^a, t_\perp^c, t)$ where $T = 2\pi/\omega$. Perhaps the appropriate tool for dealing with such time-periodic problems is Floquet theory. According to Floquet's theorem [59–61], eq (4) has solution of the form of $|\varphi(t)\rangle = e^{-i\varepsilon t/\hbar} |\phi(t)\rangle$ called the Floquet state, where ε_β stands for the quasienergy and $|\phi(t)\rangle = |\phi(t + T)\rangle$ is periodic in time. The substitution of $|\varphi(t)\rangle$ in the Schrödinger equation leads us to

$$H_F |\phi(t)\rangle = \varepsilon |\phi(t)\rangle. \quad (5)$$

where $H_F = \mathcal{H}^\xi(\mathbf{k}, t_\perp^a, t_\perp^c, t) - i\hbar \partial_t$ is the Floquet Hamiltonian. We have a periodic Floquet state $|\phi(t)\rangle$ that we can write as $|\phi(t)\rangle = \sum_{m=-\infty}^{+\infty} e^{im\omega t} |\phi_m\rangle$ and $\mathcal{H}^\xi(\mathbf{k}, t_\perp^a, t_\perp^c, t) = \sum_{n=-\infty}^{+\infty} e^{in\omega t} H_n$ using the Fourier transform. If we apply H_F to the $|\phi_n\rangle$ basis, then we express the operator H_F in terms of the infinite-dimensional Hilbert-Floquet space $\mathcal{F} = \mathcal{H} \otimes \mathcal{T}$, It is defined by the direct product of the Hilbert space \mathcal{H} in a static system and the space \mathcal{T} defined by a complete set of time-periodic functions[59, 61–64]. Therefore, we can write (5) as

$$\sum_{m=-\infty}^{+\infty} [H_{n-m} + m\hbar\omega\delta_{m,n}] |\phi_m\rangle = \varepsilon_\alpha |\phi_n\rangle. \quad (6)$$

We wish to express the quasi-energies as eigenvalues of the Floquet Hamiltonian. This is not straightforward to calculate since we have an infinity matrix equation. For this reason, we resort to describing the formulation of an effective Hamiltonian in the high-frequency driving limit. We assume a driving potential that is periodic in time, with a frequency ω that is significantly greater than the standard energy scale ϵ (or the band width) of the Hamiltonian $\mathcal{H}^\xi(\mathbf{k}, t)$, which enables us to specify a tiny paramete.

$$\lambda = \frac{\epsilon}{\hbar\omega} \ll 1. \quad (7)$$

This state strategically avoids resonances (off-resonances) between the eigenvalues of the Hamiltonian. Within this framework, light refrains from directly exciting the electrons, opting instead to modulate the states through the emission and re-absorption of virtual photons. As a result, we are able to derive an effective, time-independent Hamiltonian that aptly characterises the system.

To obtain the expression for the effective Hamiltonian, we utilize the off-resonance condition derived from eq (7), which specifies that $\varepsilon \ll \hbar\omega$. From this condition and the eigenvalue problem (6), we can rewrite the zero, one, and two Fourier components of the Floquet state with the following expression:

$$\phi_0 = \frac{1}{\varepsilon} (H_0\phi_0 + H_1\phi_{-1} + H_{-1}\phi_1), \quad (8)$$

$$\phi_{\pm 1} = \mp \frac{1}{\hbar\omega} (H_{\pm 1}\phi_0 + H_0\phi_{\pm 1} + H_{\mp 1}\phi_{\pm 2}), \quad (9)$$

$$\phi_{\pm 2} = \mp \frac{1}{2\hbar\omega} (H_{\pm 1}\phi_{\pm 1} + H_0\phi_{\pm 2} + H_{\mp 1}\phi_{\pm 3}). \quad (10)$$

The Hamiltonian Fourier modes are given by

$$\begin{aligned} H_s &= \frac{1}{T} \int_0^T \mathcal{H}^\xi(\mathbf{k}, t_\perp^a, t_\perp^c, t) e^{-is\omega t} dt, \\ &= \mathcal{H}^\xi(\mathbf{k}, t_\perp^a, t_\perp^c) \delta_{s,0} + \xi c_0 P_- \delta_{s,\xi} + \xi c_0 P_+ \delta_{s,-\xi}. \end{aligned} \quad (11)$$

Using equations (9) and (10), we obtain.

$$\phi_{\pm 1} = \mp \frac{\lambda}{\varepsilon} (H_{\pm 1}\phi_0 + H_0\phi_{\pm 1}) + \mp \frac{\lambda^2}{\varepsilon^2} H_{\mp 1} (H_{\pm 1}\phi_{\pm 1} + H_{\mp 1}\phi_{\pm 3}). \quad (12)$$

An approximate expression for the eigenvalues of the zero component of the wave function at high frequencies can be obtained by combining Eqs. (8) and (12) and keeping only the linear terms in λ (where $\lambda^2 \propto \frac{1}{\omega^2}$ is very small).

$$\left(H_0 + \frac{1}{\hbar\omega} [H_1, H_{-1}] + \mathcal{O}(1/\omega^2) \right) \phi_0 = \varepsilon \phi_0. \quad (13)$$

Finally, the time-independent effective Hamiltonian can be defined as follows:

$$H_{eff}(\mathbf{k}, t_\perp^a, t_\perp^c) = H(\mathbf{k}, t_\perp^a, t_\perp^c) + \frac{1}{\hbar\omega} [H_1, H_{-1}] + \mathcal{O}(1/\omega^2). \quad (14)$$

By applying the Fourier transform to the Fourier component of the Hamiltonian $\mathcal{H}^\xi(\mathbf{k}, t)$ from eq. (11), we obtain

$$\frac{1}{\hbar\omega} [H_1, H_{-1}] = \Delta^\xi \mathbb{1}_{2 \times 2} \otimes S_z(\phi), \quad S_z(\phi) = \begin{pmatrix} -\sin^2 \phi & 0 & 0 \\ 0 & -\cos 2\phi & 0 \\ 0 & 0 & \cos^2 \phi \end{pmatrix}. \quad (15)$$

where $\Delta^\xi = \xi c_0^2 / \hbar\omega$. Therefore, at Dirac points, particularly the corossment point, light-matter coupling gives rise to a mass term of the kind $\Delta^\xi \mathbb{1}_{2 \times 2} \otimes S_z$, which lifts the six degeneracy. Virtual photon emission and absorption, which essentially alter the static band structure, is the process this term is responsible for.

It is noteworthy that the mass term caused by off-resonance light is of the Haldane type, which breaks time-reversal symmetry in the two valleys by showing opposing signs. Under off-resonance consonance irradiation, the Hamiltonian of the bilayer $\alpha - T_3$ can be transformed into the Haldane model, even in the case of complicated nearest-neighbour hops breaking time-reversal symmetry and in the absence of sublattice potentials, as previously shown for graphene ($\alpha = 0$) and model $\alpha - T_3$ monolayer in references [20, 53, 65].

When considering terms up to $\mathcal{O}(1/\omega)$, the effective Hamiltonian (3) can be explicitly written as follows.

$$\mathcal{H}_{eff}^\xi(\mathbf{k}, t_\perp^a, t_\perp^c) = \begin{pmatrix} -\Delta^\xi \sin^2 \phi & \sin \phi f_{\mathbf{k}}^\xi & 0 & t_\perp^a & 0 & t_\perp^c \\ \sin \phi f_{\mathbf{k}}^{\xi*} & -\Delta^\xi \cos 2\phi & \cos \phi f_{\mathbf{k}}^\xi & t_\perp^c & t_\perp^a & 0 \\ 0 & \cos \phi f_{\mathbf{k}}^{\xi*} & \Delta^\xi \cos^2 \phi & 0 & t_\perp^c & t_\perp^a \\ t_\perp^a & t_\perp^c & 0 & -\Delta^\xi \sin^2 & \sin \phi f_{\mathbf{k}}^\xi & 0 \\ 0 & t_\perp^a & t_\perp^c & \sin \phi f_{\mathbf{k}}^{\xi*} & -\Delta^\xi \cos 2\phi & \cos \phi f_{\mathbf{k}}^\xi \\ t_\perp^c & 0 & t_\perp^a & 0 & \cos \phi f_{\mathbf{k}}^{\xi*} & \Delta^\xi \cos^2 \phi \end{pmatrix}. \quad (16)$$

This Hamiltonian provides an important observation: It is possible to realize the $\alpha - T_3$ bilayer sublattice within the Haldane model, either by using a laser field or by controlling the parameter α such that $\alpha = 1$. In this case, we obtain the typical Haldane Hamiltonian for the T_3 bilayer lattice, where the Hamiltonian in the low-energy case is expressed as $\text{diag}(\mathcal{H}_{eff}^\xi(\mathbf{k}, t_\perp^a, t_\perp^c)) = (-\Delta^\xi, 0, \Delta^\xi, -\Delta^\xi, 0, \Delta^\xi)$ when $\Delta^\xi = -t_2 3\sqrt{3}$ and a pure imaginary phase $\varphi = \pi/2$ is realized as described in ref[55].

Discrete symmetries, such as charge conjugation and time reversal symmetries, are crucial in many condensed matter systems, allowing electronic states and order parameters to be classified.

Time reversal symmetry is the first symmetry that we analyze. The following is the definition of the operator that reverses time symmetry: $\hat{T}_\alpha \mathcal{H}^\xi(\mathbf{k}, t_\perp^a, t_\perp^c) \hat{T}_\alpha^{-1} = \mathcal{H}^\xi(-\mathbf{k}, t_\perp^a, t_\perp^c)$. The corresponding operator, $\hat{T}_\alpha = U_\alpha \hat{\kappa}$, always includes a matrix and the complex conjugacy operator $\hat{\kappa}$. We can now check whether the effective Hamiltonians Aligned $\mathcal{H}_{eff}^\xi(\mathbf{k}, t_\perp^a, 0)$ and Cyclic $\mathcal{H}_{eff}^\xi(\mathbf{k}, 0, t_\perp^c)$ are invariant under the \hat{T}_α time-reversal operation. After completing the calculation, we find.

$$\hat{T}_0 \mathcal{H}_{eff}^{\xi, \alpha=0}(\mathbf{k}, t_\perp^a, 0) \hat{T}_0^{-1} \neq \mathcal{H}_{eff}^{\xi, \alpha=0}(-\mathbf{k}, t_\perp^a, 0), \quad \hat{T}_1 \mathcal{H}_{eff}^{\xi, \alpha=1}(\mathbf{k}, t_\perp^a, 0) \hat{T}_1^{-1} \neq \mathcal{H}_{eff}^{\xi, \alpha=1}(-\mathbf{k}, t_\perp^a, 0). \quad (17)$$

$$\hat{T}_0 \mathcal{H}_{eff}^{\xi, \alpha=0}(\mathbf{k}, 0, t_\perp^c) \hat{T}_0^{-1} \neq \mathcal{H}_{eff}^{\xi, \alpha=0}(-\mathbf{k}, 0, t_\perp^c), \quad \hat{T}_1 \mathcal{H}_{eff}^{\xi, \alpha=1}(\mathbf{k}, 0, t_\perp^c) \hat{T}_1^{-1} \neq \mathcal{H}_{eff}^{\xi, \alpha=1}(-\mathbf{k}, 0, t_\perp^c). \quad (18)$$

In this case, the time reversal operators in Hamiltonian Aligned $U_\alpha = 0$ and $U_\alpha = 1$ are specified as follows for the A-A graphene bilayer and the die bilayer, respectively:

$$U_{\alpha=0} = \begin{pmatrix} 0 & 1 \\ 1 & 0 \end{pmatrix} \otimes \begin{pmatrix} 1 & 0 & 0 \\ 0 & 0 & -1 \\ 0 & 1 & 0 \end{pmatrix}, \quad U_{\alpha=1} = \begin{pmatrix} 1 & 0 \\ 0 & 1 \end{pmatrix} \otimes \begin{pmatrix} 0 & 0 & 1 \\ 0 & -1 & 0 \\ 1 & 0 & 0 \end{pmatrix}. \quad (19)$$

The time reversal operators for the Hamiltonian Cyclic $U_{\alpha=0}$ and $U_{\alpha=1}$ are as follows for the A-B stacked graphene bilayer and the AB-BC-CA stacked die bilayer, respectively:

$$U_{\alpha=0} = \begin{pmatrix} 0 & 0 & 0 & 1 & 0 & 0 \\ 0 & 0 & 0 & 0 & 0 & 1 \\ 0 & 0 & 0 & 0 & -1 & 0 \\ 1 & 0 & 0 & 0 & 0 & 0 \\ 0 & 0 & -1 & 0 & 0 & 0 \\ 0 & 1 & 0 & 0 & 0 & 0 \end{pmatrix}, \quad U_{\alpha=1} = \begin{pmatrix} 0 & 0 & 0 & 0 & 0 & 1 \\ 0 & 0 & 0 & 0 & -1 & 0 \\ 0 & 0 & 0 & 1 & 0 & 0 \\ 0 & 0 & -1 & 0 & 0 & 0 \\ 0 & 1 & 0 & 0 & 0 & 0 \\ 1 & 0 & 0 & 0 & 0 & 0 \end{pmatrix}. \quad (20)$$

The lack of time-reversal symmetry in Hamiltonian alignment $\mathcal{H}_{eff}^{\xi}(\mathbf{k}, t_{\perp}^a, 0)$ and Hamiltonian cyclic $\mathcal{H}_{eff}^{\xi}(\mathbf{k}, 0, t_{\perp}^c)$ is due to circular polarization vectors breaking the time-reversal symmetry enforced by a mass term, as demonstrated in equations (17) and (18). Cramer's theorem, which proves that the symmetry condition is broken, leads to a gap opening at valley K or K'. We will discuss this in the section on quasi-energy.

Next, we will discuss charge conjugation symmetry, also known as particle-hole symmetry (C symmetry), which has the following definition: $\hat{C}\mathcal{H}^{\xi}(\mathbf{k}, t_{\perp}^a, t_{\perp}^c)\hat{C}^{-1} = -\mathcal{H}^{\xi}(-\mathbf{k}, t_{\perp}^a, t_{\perp}^c)$. In the matrix form $\hat{C} = M_{\alpha}\hat{\kappa}$, the appropriate operator is defined.

By applying the aforementioned operator to the effective Hamiltonians for alignment $\mathcal{H}_{eff}^{\xi}(\mathbf{k}, t_{\perp}^a, 0)$ and cyclic $\mathcal{H}_{eff}^{\xi}(\mathbf{k}, 0, t_{\perp}^c)$ ($\alpha = 0$ and $\alpha = 1$), it can be demonstrated that the particle-hole symmetry invariance is expressed in the Hamiltonian as:

$$\hat{C}_0\mathcal{H}_{eff}^{\xi, \alpha=0}(\mathbf{k}, t_{\perp}^a, 0)\hat{C}_0^{-1} = -\mathcal{H}_{eff}^{\xi, \alpha=0}(-\mathbf{k}, t_{\perp}^a, 0), \quad \hat{C}_1\mathcal{H}_{eff}^{\xi, \alpha=1}(\mathbf{k}, t_{\perp}^a, 0)\hat{C}_1^{-1} = -\mathcal{H}_{eff}^{\xi, \alpha=1}(-\mathbf{k}, t_{\perp}^a, 0). \quad (21)$$

$$\hat{C}_0\mathcal{H}_{eff}^{\xi, \alpha=0}(\mathbf{k}, 0, t_{\perp}^c)\hat{C}_0^{-1} = -\mathcal{H}_{eff}^{\xi, \alpha=0}(-\mathbf{k}, 0, t_{\perp}^c), \quad \hat{C}_1\mathcal{H}_{eff}^{\xi, \alpha=1}(\mathbf{k}, 0, t_{\perp}^c)\hat{C}_1^{-1} = -\mathcal{H}_{eff}^{\xi, \alpha=1}(-\mathbf{k}, 0, t_{\perp}^c). \quad (22)$$

where $M_{\alpha=1}$ and $M_{\alpha=0}$ represent the operators in the aligned effective Hamiltonian for AA-BB-CC bilayer die and A-A bilayer graphene, respectively.

$$M_{\alpha=1} = \tau_z \otimes \mathbb{1}_{3 \times 3}, \quad M_{\alpha=0} = i\tau_y \otimes \begin{pmatrix} 1 & 0 & 0 \\ 0 & 0 & 1 \\ 0 & 1 & 0 \end{pmatrix}. \quad (23)$$

The charge conjugation operators for the cyclic Hamiltonians, $M_{\alpha=0}$ (A-B graphene) and $M_{\alpha=1}$ (AB-BC-CA dice), are given below

$$M_{\alpha=1} = i\tau_y \otimes \mathbb{1}_{3 \times 3}, \quad M_{\alpha=0} = i\tau_y \otimes \begin{pmatrix} 1 & 0 & 0 \\ 0 & 0 & 1 \\ 0 & 1 & 0 \end{pmatrix}. \quad (24)$$

$\mathbb{1}_{3 \times 3}$, the identity matrix, along with τ_y and τ_z , are Pauli matrices. A band of energy $\varepsilon(k)$ will have a partner band of energy $-\varepsilon(-k)$, according to relations (21) and (22). This symmetry proves that the six-band system consists of a flat energy band shifted by t_{\perp} with partner $-t_{\perp}$. It is important to note that the Hamiltonian is traceless. Radiation will therefore not affect the flat band in the dice lattice. Therefore, for all values of α , the sum of the energies of the bands will always be zero.

A. Quasienergy

We can now determine the eigenvalues $\varepsilon_m(k)$ of $\mathcal{H}_{eff}^{\xi}(\mathbf{k}, t_{\perp}^a, t_{\perp}^c)$. These represent the structure of the quasi-energy band of off-resonance. The characteristic equation of the eigenvalue problem for the Hamiltonian $\mathcal{H}^{\xi}(\mathbf{k}, 0, t_{\perp}^c)$ is very complex, so we solve it numerically. Below, we discuss the results obtained to draw the electronic structure. The characteristic equation of the Hamiltonian $\mathcal{H}^{\xi}(\mathbf{k}, t_{\perp}^a, 0)$ can be summarized as a reduced **depressed cubic equation**: $(\varepsilon_{\mathbf{m}}(\mathbf{k}) \pm \mathbf{t}_{\perp})^3 + \mathbf{p}(\varepsilon_{\mathbf{m}}(\mathbf{k}) \pm \mathbf{t}_{\perp}) + \mathbf{q} = \mathbf{0}$. The solutions of this equation give us the quasi-energies in the form:

$$\varepsilon_m^s(k) = st_{\perp} + 2\sqrt{\frac{-p}{3}} \cos\left(\frac{1}{3} \arccos\left(\frac{3q}{2p}\sqrt{\frac{3}{-p}}\right) - \frac{2\pi m}{3}\right). \quad (25)$$

where

$$p = - \left[|f_{\mathbf{k}}^{\xi}|^2 + \frac{\Delta \xi^2}{8} (5 + 3 \cos 4\phi) \right], \quad q = -\frac{\Delta \xi^2}{8} \sin 2\phi \sin 4\phi. \quad (26)$$

We consider two cases: ($m = 0, 1, 2$ and $s = 1$) and ($m = 0, 1, 2$ and $s = -1$), which represent the quasi-energies of the conduction and valence bands, respectively. Due to interlayer coupling, these quasi-energies exhibit a shift from a single point near $t_{\perp} = 0$ to two points located close to the band crossing points at st_{\perp} . This phenomenon leads to the formation of a flat band in the conduction band at t_{\perp} and another in the valence band at $-t_{\perp}$. Off-resonance radiation significantly modifies the band structure of the undriven $\alpha - T_3$ bilayer lattice. It depends on both α and d near the Dirac point and specifically at the band crossing points. When the parameter α is varied, interesting physical properties are observed, which will be investigated further. For clarity and consistency, I propose using the following simplified notation for quasi-particle energies in subsequent calculations: $\varepsilon_1(k) = \varepsilon_2^{-1}(k)$, $\varepsilon_2(k) = \varepsilon_1^{-1}(k)$, $\varepsilon_3(k) = \varepsilon_0^{-1}(k)$, $\varepsilon_4(k) = \varepsilon_2^1(k)$, $\varepsilon_5(k) = \varepsilon_1^1(k)$, and $\varepsilon_6(k) = \varepsilon_1^0(k)$.

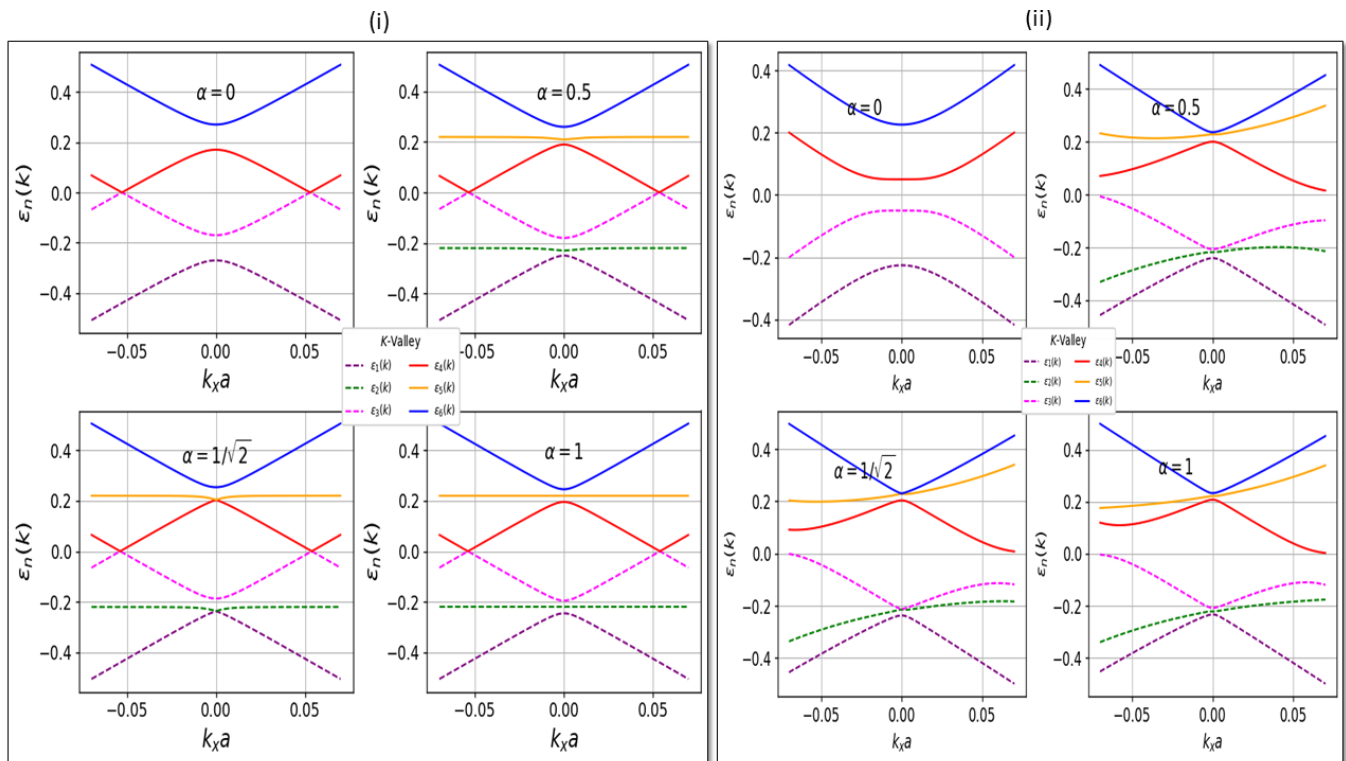


FIG. 2. The influence of the α parameter on the quasi-energy dispersion in the K-valley of an aligned stack (i) and a cyclic stack (ii) is illustrated by the graph presented. The results obtained highlight the effect of this parameter on dispersion for different values of α , considering circularly polarized light with an energy of $\Delta = 50\text{meV}$

In this paragraph, we explore the evolution of topological band structures by varying α continuously. We will analyze the band structures of an $\alpha - T_3$ bilayer with aligned and cyclic stacking, illustrated in Figures 2(i) and 2(ii). The choice of the coupling strengths between the different sublattices of the two layers seems to influence the energy spectrum of the $\alpha - T_3$ bilayer lattice. In the aligned stack, the bands are dispersed and flat, while the coupling between the layers in the cyclic stack induces waviness in the flat bands. We consider the system to be irradiated with right-circularly polarized radiation. The amplitude and frequency are chosen such that $\Delta = 50\text{meV}$. Equation (16) provides a description of the two non-equivalent incommensurate stackings, both for the case with and without the inclusion of circular polarization.

In bilayer geometry, the effect of circularly polarized radiation on the band structure of the system manifests itself in two primary ways for the two stacking configurations of the $\alpha - T_3$ bilayer lattice, at $\alpha = 0$ and $\alpha = 1$. Firstly, it leads to the breaking of time-reversal symmetry, which in turn results in the complete lifting of the triple degeneracy of the valence and conduction bands at the Dirac point ($k = 0$) through the opening of a gap. However, the scenario

corresponding to $\alpha = 1/\sqrt{2}$ exhibits distinct behavior. Here, the valence and conduction bands exhibit a flat and corrugated band topology in both the aligned and cyclic stackings. Notably, a topological phase transition occurs at $\alpha = 1/\sqrt{2}$, as previously observed in an $\alpha - T_3$ monolayer [65]. Secondly, the circular radiation deforms the flat and corrugated band near the Dirac point ($k = 0$) for intermediate values of α ($0 < \alpha < 1$). Interestingly, the particle-hole symmetry is broken in both the aligned and cyclic stackings. However, this symmetry remains preserved for graphene ($\alpha = 0$) and the dice lattice ($\alpha = 1$).

For instance, in an irradiated dice lattice with aligned stacking, the energy spectrum is described by the equation: $st \pm (|f_{\mathbf{k}}^\xi|^2 + \Delta^2)^{1/2}$, where st . Notably, this equation demonstrates that the "flatness" of the cyclic stacking's characteristic flat and wavy band is preserved even under high-frequency radiation. It is important to note the particle-hole transformation, where the energy of an electron $\varepsilon(k)$ is replaced by the energy of a hole $-\varepsilon(-k)$.

Circular polarization breaks the system's time-reversal symmetry, causing the six bands to split and leading to the creation of a finite zero-energy gap. The alpha parameter determines whether this gap is closed in the conduction and valence bands. This closure can be derived by obtaining the eigenvalues at a Dirac point ($k = 0$) in the aligned stacking. The formula for the gap is $\delta = \Delta/2(1 - 3 \cos \phi)$, as shown in reference [55]. Including a Haldane flux instead of circular polarization preserves the insulating state in the cyclic stacking. In the absence of radiation, Kramer's degeneracy is ensured by time-reversal symmetry, regardless of the alpha value. However, introducing radiation, which breaks time-reversal symmetry, lifts this degeneracy.

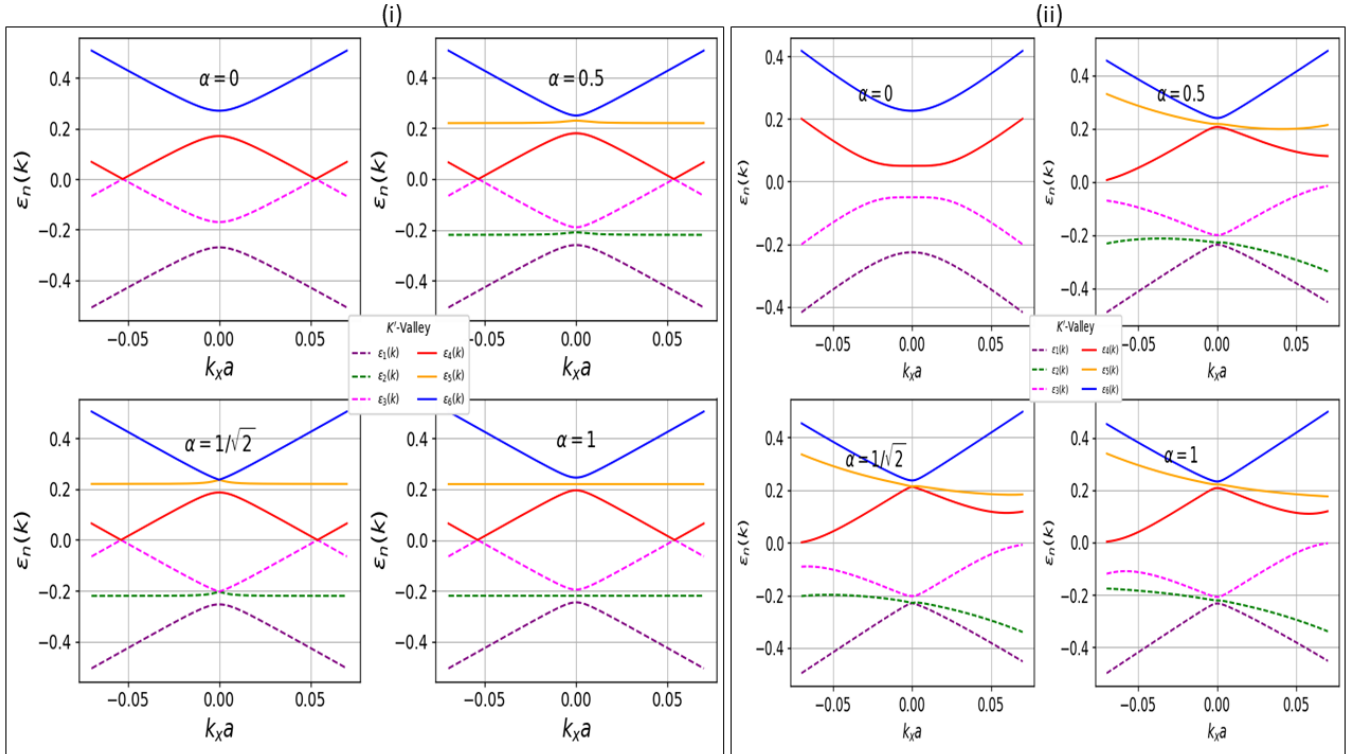


FIG. 3. We repeat figure 2 for the K'-valley

Figures 3(i) and 3(ii) show the quasiparticle energy dispersion for the K' valley in both aligned and cyclic stacking configurations, using the same parameters. Notably, the conduction and valence bands below the flat band touch the deformed flat band at $\alpha = 1/\sqrt{2}$. Interestingly, the behavior observed in the K' valley can be replicated in the K valley by simply inverting the radiation polarization Δ to $-\Delta$ for the aligned stack.

The band topology remains unchanged if the energy gap of the conduction and valence bands does not close and reopen during continuous adjustment of the parameter. In this case, we observed that one of the gaps closes at $\alpha = 1/\sqrt{2}$ and reopens at $\alpha \neq 1/\sqrt{2}$. Therefore, we anticipate a band topology transition at $\alpha = 1/\sqrt{2}$. In this context, a change in Berry curvature and orbital magnetic moment can be used to identify whether the system undergoes a topological transition.

B. Berry Curvature

In quantum systems, particularly those with Bloch bands, Berry curvature emerges as a significant geometric property. This curvature plays a crucial role in various physical phenomena, especially around a Dirac point, including the anomalous quantum Hall effect and topological transport effects. When considering an adiabatic system –where changes occur slowly enough for the quantum state to continuously adapt –the electron traversing k -space around the Dirac point accumulates a geometric phase in addition to the dynamical phase. This geometric phase is intimately linked to the concepts of Berry connection and Berry curvature. In momentum space, the Berry connection acts as a vector potential, denoted by $\mathbf{A}_m^\xi(\mathbf{k}) = i \langle u_m^\xi(\mathbf{k}) | \nabla_{\mathbf{k}} | u_m^\xi(\mathbf{k}) \rangle$. Here, $|u_m^\xi(\mathbf{k})\rangle = e^{-i\mathbf{k}\mathbf{r}} |\phi_m^\xi(\mathbf{k})\rangle$ represents the periodic part of the n th occupied band's Bloch function in valley ξ . The Berry curvature, particularly its z component denoted by $\Omega_m^\xi(\mathbf{k}) = (\nabla_{\mathbf{k}} \times \mathbf{A}_m^\xi(\mathbf{k}))_z$, is derived from this connection. This z component, analogous to the magnetic field in real space, exhibits gauge invariance. More specifically, the z component of the Berry curvature has been calculated numerically (as detailed in [67]) and can be expressed as follows.

$$\Omega_m^\xi(\mathbf{k}) = -2\hbar^2 \mathcal{J}_m \sum_{m' \neq m} \frac{\langle u_m^\xi(\mathbf{k}) | v_x | u_{m'}^\xi(\mathbf{k}) \rangle \langle u_{m'}^\xi(\mathbf{k}) | v_y | u_m^\xi(\mathbf{k}) \rangle}{(\varepsilon_m^\xi(\mathbf{k}) - \varepsilon_{m'}^\xi(\mathbf{k}))^2}, \quad (27)$$

The summation extends over all n occupied bands, with the term $v_i = \hbar^{-1} \nabla_{k_i} \mathcal{H}^\xi \text{eff}(\mathbf{k}, t_\perp^a, t_\perp^c)$ representing the effective velocity operator in a specific direction ($i = x, y$). In essence, Berry curvature describes how an electron's wave function responds to the curvature of its energy band as its momentum varies within a material. However, as shown in Eq. (27), the Berry curvature becomes singular when the energy levels of two or more states are degenerate. In systems exhibiting symmetries under spatial inversion (\mathcal{I}), particle-hole transformation (\mathcal{C}), and time reversal (\mathcal{T}), the Berry curvature transforms according to specific rules: $\mathcal{I}^{-1} \Omega_m(\mathbf{k}) \mathcal{I} = \Omega_m(-\mathbf{k})$, $\mathcal{C}^{-1} \Omega_{\bar{m}}(\mathbf{k}) \mathcal{C} = -\Omega_m(-\mathbf{k})$, and $\mathcal{T}^{-1} \Omega_m(\mathbf{k}) \mathcal{T} = -\Omega_m(-\mathbf{k})$. In crystals that possess all three symmetries simultaneously, the Berry curvature vanishes identically across the entire Brillouin zone. Conversely, in systems where any of these symmetries are broken, the Berry curvature can become significant, playing a crucial role in their electronic properties. Where the label \bar{m} indicates the band of energy $-\varepsilon_m(-k)$.

Irradiation plays a critical role in shaping the topological properties of $\alpha - T_3$ bilayer lattices with aligned and cyclic stacking geometries. These lattices exhibit six distinct bands with non-trivial topological character for each stacking type. As shown in Figures 2(i) and 2(ii), these bands comprise the flat (wavy) bands $\varepsilon_2(k)$ and $\varepsilon_5(k)$ for aligned (cyclic) stacking, respectively, alongside the dispersive bands $\varepsilon_1(k)$, $\varepsilon_3(k)$, $\varepsilon_4(k)$, and $\varepsilon_6(k)$ common to both configurations. To investigate the system's topological evolution, we systematically varied the α parameter from 0 to 1. The non-zero Berry curvature, arising from the curvature of the bands, is responsible for inducing the topological character. Figures 4(i) and 4(ii) illustrate the K -valley Berry curvature behavior for irradiated aligned and cyclically stacked $\alpha - T_3$ bilayers (considering a fixed Δ value of 50 meV). Notably, the Berry curvature for individual bands becomes non-vanishing due to the breaking of time-reversal symmetry. In all observed cases, $\Omega_m(\mathbf{k})$ exhibits a tendency to concentrate near the valley's end.

For aligned stacking, the Berry curvature remains invariant compared to single-layer irradiated $\alpha - T_3$ lattices. This phenomenon can be attributed to the fact that the bands of bilayer lattices simply encompass those of the single layer, experiencing a shift mediated by the interlayer coupling strength, t_\perp . The Berry curvature itself depends on factors beyond just the band dispersion. Interestingly, we observe that the positive dispersion term, which incorporates the energy bands, consistently leads to negative Berry curvature across all α values. Conversely, inferring topological characteristics from the negative dispersion term's $\Omega_m(k)$ behavior proves to be more challenging. The positive dispersion term, however, exhibits non-monotonic behavior. At $\alpha = 0$, it's positive and peaks at $k = 0$. As α increases to 0.4, a cusp-like structure with a negative peak value emerges. When α reaches 0.8, the Berry curvature strengthens significantly and becomes positive. This positive character persists even with further increases in α to 1. Notably, $\Omega_m(k)$ exhibits a sign change around $\alpha = 1/\sqrt{2}$, which could potentially serve as a signature of a topological transition.

Within the range $0 < \alpha < 1$, the Berry curvature associated with the flat band acquires a non-zero value due to the breaking of particle-hole symmetry by the external irradiation. However, for the dice lattice ($\alpha = 1$), the flat band's contribution to the Berry curvature at $\Omega_m(k)$ vanishes entirely. This is because the irradiation at this specific α value is incapable of breaking particle-hole symmetry. Notably, the total Berry curvature, which is the sum of individual contributions from all bands for a given k -value, remains zero. This phenomenon, known as local conservation of Berry curvature, ensures that curvature gained in one band is counterbalanced by curvature of opposite sign in another.

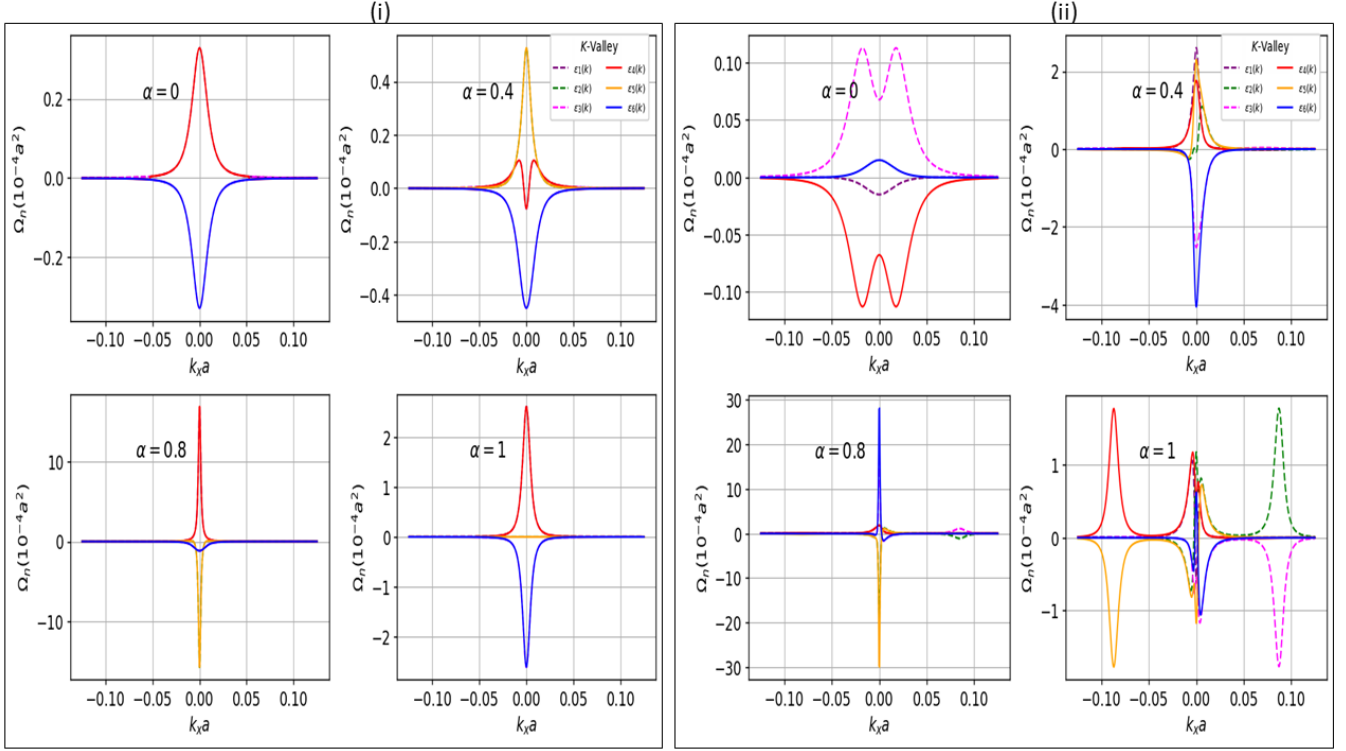


FIG. 4. Berry curvature curves $\Omega_m^{+1}(\mathbf{k})$ for aligned (i) and cyclic (ii) stacking near the K-valley are plotted for different values of α , namely $\alpha = 0$, $\alpha = 0.4$, $\alpha = 0.8$, and $\alpha = 1$. We consider irradiation of the $\alpha - T_3$ bilayer lattice with circularly polarized light of amplitude $\Delta = 50$ meV

The Berry curvature exhibits complex behavior in the cyclically stacked $\alpha - T_3$ lattice. For both the conduction and valence bands, $\Omega_m(k)$ changes sign across all α values, making it challenging to directly infer topological characteristics from their behavior. At $\alpha = 0$, the Berry curvature of the valence band $\varepsilon_1(k)$ is negative, while that of the conduction band $\varepsilon_4(k)$ is positive, forming a cup-like structure at $k = 0$. It displays non-monotonic behavior as α increases to 0.4. Interestingly, for both corrugated bands $\varepsilon_2(k)$ and $\varepsilon_5(k)$, $\Omega_m(k)$ transitions from negative to positive at $\alpha = 0.4$. An intriguing observation is the sign change of $\Omega_m(k)$ around $\alpha = 1/\sqrt{2}$ for bands $\varepsilon_3(k)$ and $\varepsilon_1(k)$ at $\alpha = 0.8$. This behavior, previously observed in aligned stacks and single-layer $\alpha - T_3$ lattices, could potentially indicate a topological signature, similar to the previously reported topological phase transition in Haldane term bilayer cyclic $\alpha - T_3$ stacks [67]. Furthermore, the corrugated bands $\varepsilon_2(k)$ and $\varepsilon_5(k)$ also exhibit a sign change in $\Omega_m(k)$ at $\alpha = 1/\sqrt{2}$. In fact, for $\alpha = 1$, all bands display non-monotonic behavior with sign changes. Notably, the contribution of the corrugated band to $\Omega_m(k)$ remains non-zero and reaches its maximum value at $k = 0$ and $k_x a \approx 0.085$. However, external radiation at this α value fails to break the particle-hole symmetry. For the range $0 < \alpha \leq 1$, the Berry curvature associated with the corrugated bands ($\varepsilon_2(k)$ and $\varepsilon_5(k)$) becomes non-zero, breaking the particle-hole symmetry. This effect is absent only at $\alpha = 1$, where the local conservation of Berry curvature is maintained due to the cancellation of individual band contributions, resulting in a total Berry curvature of zero for any given k -value.

We investigated the Berry curvature, $\Omega_m(k)$, for both aligned and cyclically stacked $\alpha - T_3$ bilayer lattices. For the K(K') valley, where $\Omega_m(k = 0)$ reaches its maximum value, we plotted $\Omega_m(k)$ at $k = 0$ across the entire α range, as shown in FIG.5.

For aligned $\alpha - T_3$ bilayer lattices in the K valley, the Berry curvatures corresponding to the flat bands ($\varepsilon_{2,5}(k)$) and the bands with negative dispersion ($\varepsilon_1(k) + t < 0$ et $\varepsilon_4(k) - t < 0$) diverge as α approaches $1/\sqrt{2}$. In contrast, the curvatures for the bands with positive dispersion ($\varepsilon_3(k) + t > 0$ and $\varepsilon_6(k) - t > 0$) remain finite, as illustrated in FIG.5(i). This divergence stems from the fact that the flat bands and the bands with negative dispersion touch at $k = 0$ when $\alpha = 1/2$. This degeneracy at this point introduces a singularity in the Berry curvature. Additionally, the Berry curvatures for the flat bands (bands with negative dispersion) change sign, transitioning from positive (negative) to negative (positive) as α varies around $\alpha = 1/\sqrt{2}$, constituting a topological signature.

For the K' valley, the Berry curvature remains finite for the band with negative dispersion, while the curvature

corresponding to the positive band and the flat bands exhibits a divergence at $\alpha = 1/\sqrt{2}$. This behavior arises from the degeneracy of the bands with positive dispersion and the flat bands at $k = 0$. The Berry curvatures for the bands with positive dispersion and the flat bands change their signs respectively around $\alpha = 1/2$, as illustrated in FIG.5(ii).

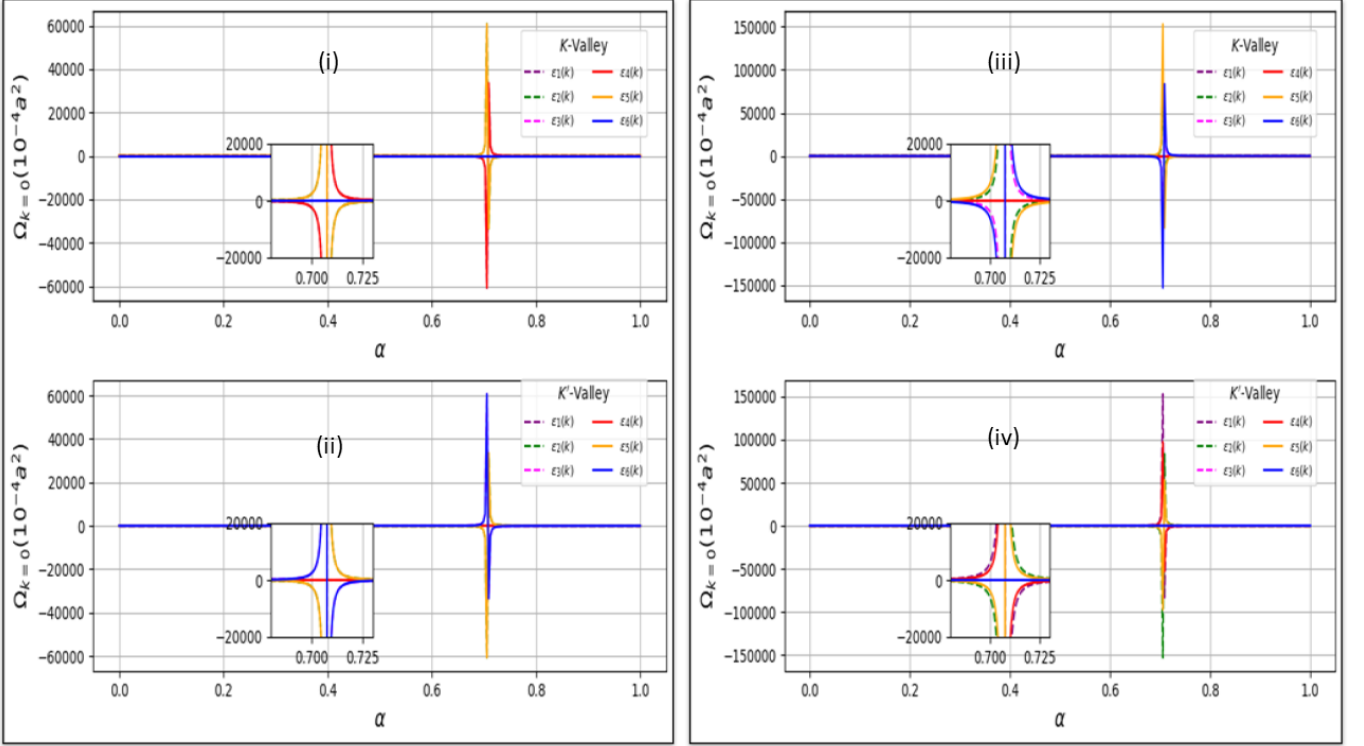


FIG. 5. The maximum value of $\Omega(k = 0)$ at $k = 0$ is plotted as a function of α for (i) the K-valley and (ii) the K'-valley of the aligned stack, as well as for (iii) the K-valley and (iv) the K'-valley of the cyclic stack. Here, we consider $\Delta = 50$ meV. In the K (K') valley, $\Omega(k = 0)$ for the band change sign discontinuously through $\alpha = 1/\sqrt{2}$ while $\Omega(k = 0)$ for the conduction (valence) band decreases (increases) monotonically as illustrated in the inset. The change in sign of the Berry curvature through $\alpha = 1/\sqrt{2}$ can be seen as a topological signature

In the K valley of cyclically stacked $\alpha - T_3$ bilayer lattices, the Berry curvatures exhibit divergences for the wavy bands ($\varepsilon_{5,2}$), as well as for the valence band $\varepsilon_3(k)$ and conduction band $\varepsilon_6(k)$ at $\alpha = 1/\sqrt{2}$. In contrast, the Berry curvatures remain finite for the valence band $\varepsilon_1(k)$ and conduction band $\varepsilon_4(k)$, as illustrated in FIG.5(iii). These divergences at $\alpha = 1/\sqrt{2}$ arise from band crossings at $k = 0$. Additionally, $\Omega(k = 0)$ for the wavy bands ($\varepsilon_{2,5}(k)$), as well as for the valence band $\varepsilon_3(k)$ and conduction band $\varepsilon_6(k)$, changes sign (+ to - or - to +) as α varies around $\alpha = 1/2$, potentially indicating a topological signature.

For the K' valley, the Berry curvature remains finite for the conduction band $\varepsilon_6(k)$ and valence band $\varepsilon_3(k)$, while exhibiting divergences at $\alpha = 1/\sqrt{2}$ for the valence band $\varepsilon_1(k)$, conduction band $\varepsilon_4(k)$, and the wavy bands. These divergences stem from the degeneracy of the wavy band $\varepsilon_2(k)$ and conduction band $\varepsilon_1(k)$ at $k = 0$, as well as the degeneracy of the wavy band $\varepsilon_5(k)$ and valence band $\varepsilon_4(k)$. The Berry curvatures for the wavy bands $\varepsilon_2(k)$ and $\varepsilon_5(k)$, as well as for the conduction band $\varepsilon_1(k)$ and valence band $\varepsilon_4(k)$, change sign around $\alpha = 1/\sqrt{2}$, as shown in FIG.5(iv).

C. Orbital Magnetic moment

An intriguing concept in condensed matter physics is the orbital magnetic moment (OMM) associated with Bloch electrons. Bloch electrons, represented by wave packets within Bloch bands, typically exhibit self-rotation around their centre of mass, giving rise to an intrinsic orbital magnetic moment. This OMM has similarities to the behaviour of electron spin. In principle, by studying the magnetic circular dichroism spectrum, various information can be extracted from OMM [68, 69], so it can be treated as a physical observable. The general expression for OMM is given

by

$$\mathbf{m}_m^\xi(\mathbf{k}) = -i(e/2\hbar) \langle \nabla_{\mathbf{k}} u_m^\xi(\mathbf{k}) | (H_{eff}^\xi(\mathbf{k}) - \varepsilon_m(\mathbf{k})) | \nabla_{\mathbf{k}} u_m^\xi(\mathbf{k}) \rangle, \quad (28)$$

We aim to determine the simplest expression for the orbital magnetic moment (OMM). Additionally, by differentiating the eigenvalue equation $\mathcal{H}^\xi_{eff}(\mathbf{k}) |u_m^\xi(\mathbf{k})\rangle = \varepsilon_m(\mathbf{k}) |u_m^\xi(\mathbf{k})\rangle$ with respect to \mathbf{k} and applying the identity, we obtain

$$\langle \nabla_{\mathbf{k}} u_{m'}^\xi(\mathbf{k}) | u_m^\xi(\mathbf{k}) \rangle = \frac{\langle u_{m'}^\xi(\mathbf{k}) | \nabla_{\mathbf{k}} \mathcal{H}^\xi_{eff}(\mathbf{k}) | u_m^\xi(\mathbf{k}) \rangle}{\varepsilon_{m'}(\mathbf{k}) - \varepsilon_m(\mathbf{k})}, \quad (29)$$

Through the inclusion of the unit operator $1 = \sum_m |u_m^\xi(\mathbf{k})\rangle \langle u_m^\xi(\mathbf{k})|$ and Eq.(29) into Eq.(28), we can reformulate the z -component of Eq.(28) as follows.

$$m_m^\xi(\mathbf{k}) = -\hbar e \mathcal{I} \mathbf{m} \sum_{m' \neq m} \frac{\langle u_m^\xi(\mathbf{k}) | v_x | u_{m'}^\xi(\mathbf{k}) \rangle \langle u_{m'}^\xi(\mathbf{k}) | v_y | u_m^\xi(\mathbf{k}) \rangle}{\varepsilon_m^\xi(\mathbf{k}) - \varepsilon_{m'}^\xi(\mathbf{k})}. \quad (30)$$

The behavior of the OMM is analyzed within the framework of Equation (30) for irradiated $\alpha - T_3$ lattices with both aligned and cyclic stacking arrangements (Figures 6(i) and 7(i) depict the OMM distribution for the K valley). Notably, the existence of a non-zero OMM for the Hamiltonian (16) in these two stacking configurations can be established through fundamental symmetry transformation relations of the OMM. Under inversion (\mathcal{I}), particle-hole transformation (\mathcal{C}), and time-reversal (T) operations, the OMM transforms as $\mathcal{I}^{-1} m_m(k) \mathcal{I} = m_m(-k)$, $\mathcal{C}^{-1} m_{\bar{m}}(k) \mathcal{C} = m_m(-k)$, and $T^{-1} m_m(k) T = -m_m(-k)$, respectively. Therefore, the existence of a non-zero $m(k)$ requires the breaking of at least one of these symmetries. Interestingly, the OMM distribution exhibits a peak around the valley edge ($k \approx 0$), similar to the Berry curvature. However, distinct features differentiate the OMM distribution from that of the Berry curvature, suggesting the presence of additional mechanisms influencing the OMM in irradiated $\alpha - T_3$ lattices.

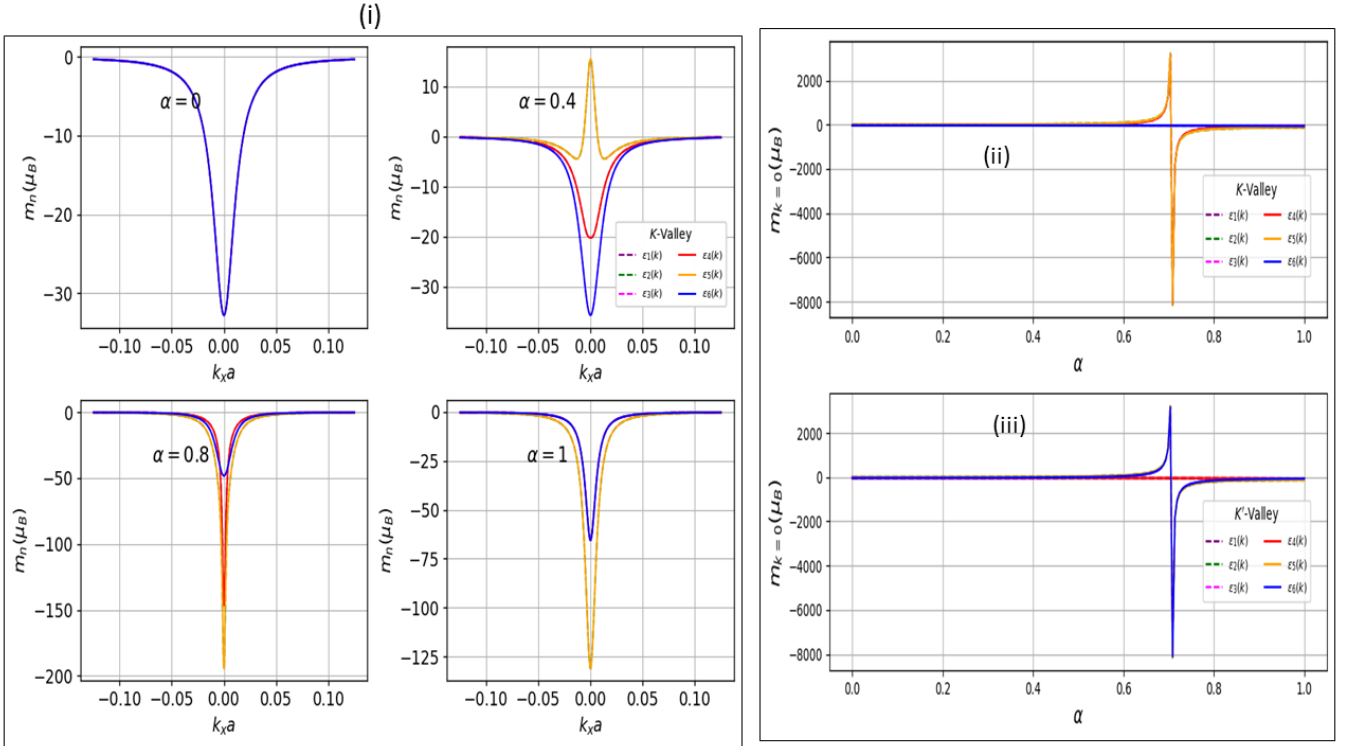


FIG. 6. Variation of the orbital magnetic moment in the bilayer aligned stack $\alpha - T_3$ as a function of the wave vector k_x around the valley K: (i) for different values of the parameter α , with $\Delta = 50\text{meV}$, based on the calculations of Eq. (30); (ii) evolution of the maximum value of $m(k)$ in $k = 0$ as a function of α in the K valley, showing discontinuities in the sign of the orbital magnetic moment associated with the flat band $\varepsilon_2(k)$, the valence band $\varepsilon_1(k)$, and the conduction band $\varepsilon_4(k)$ at $\alpha = 1/\sqrt{2}$; (iii) the same analysis in the K' valley where the roles of the $\varepsilon_1(k)$ and $\varepsilon_4(k)$ bands are replaced by $\varepsilon_3(k)$ and $\varepsilon_6(k)$, respectively.

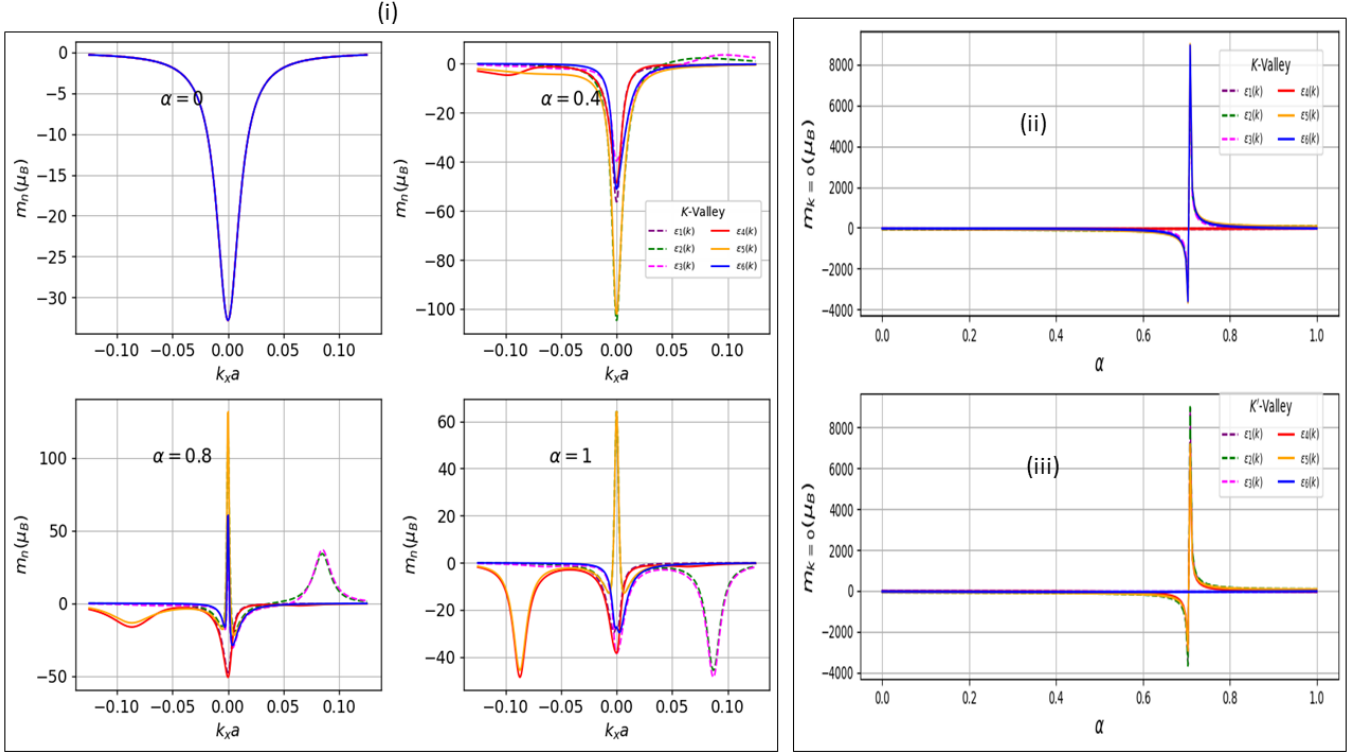


FIG. 7. Orbital Magnetic Moment variation in cyclic Stacking of $\alpha - T_3$ bilayer as a function of k_x momentum (i) around the K valley for different α parameters. variation of the maximum value of $m(k)$ at $k = 0$ for cyclic Stacking as a function of α : (ii) In the K valley, with discontinuous changes in the signals from the wavy band $\varepsilon_2(k)$, band $\varepsilon_5(k)$, valence band $\varepsilon_3(k)$, and conduction band $\varepsilon_6(k)$ at $\alpha = 1/\sqrt{2}$, and (iii) In the K' Valley, where the role of the conduction band $\varepsilon_4(k)$ and valence band $\varepsilon_1(k)$ is replaced by the valence band $\varepsilon_3(k)$ for $\varepsilon_6(k)$, with $\Delta = 50$ meV.

In aligned $\alpha - T_3$ bilayer systems, when time-reversal symmetry is broken, it results in non-zero OMMs. Specifically, for the values $\alpha = 0$ and $\alpha = 1$, as illustrated in Figure 6(i), the OMMs associated with the conduction and valence bands are found to be negative and coincide due to particle-hole symmetry. One fascinating observation is that the OMM linked to non-vanishing flat bands at $\alpha = 1$ shows an opposite sign compared to that observed in the Berry curvature. This observation sheds light on the unique behavior of OMMs in these systems. Within the intermediate α regime ($0 < \alpha < 1$), the broken time-reversal symmetry leads to distinct Orbital Magnetic Moment (OMM) values for individual bands in $\alpha - T_3$ bilayers. This observation stands in contrast to monolayer systems, where both time-reversal and particle-hole symmetries have been observed to be broken simultaneously. We present the variation of $m(k = 0)$ with α for the two valleys in Fig.6(ii)-(iii) to explore the topological characteristics of the OMM. For the K valley, the OMMs corresponding to the flat bands $\varepsilon_2(k)$ and $\varepsilon_5(k)$ as well as the conduction band $\varepsilon_4(k)$ and the valence band $\varepsilon_1(k)$ change their signs respectively at $\alpha = 1/\sqrt{2}$. In contrast, the one associated with the conduction band $\varepsilon_6(k)$ and the valence band ε_3 is monotone with respect to α . For the K' valley, the roles of the conduction bands $\varepsilon_4(k)$ and valence $\varepsilon_1(k)$ are reversed, respectively with the valence band $\varepsilon_3(k)$ and the conduction band $\varepsilon_6(k)$. Let's now analyse the behaviour of the OMMs in the cyclic stacking of $\alpha - T_3$ bilayers, as mentioned above. The time inversion is broken, resulting in non-zero OMMs, as illustrated in Fig.7(i). The OMMs corresponding to the conduction and valence bands are negative for $\alpha = 0$. For $\alpha = 1$, the OMMs for the conduction and valence bands are negative, except for the corrugated bands, which are positive near $k_x \approx 0$ and negative at $k_x a \approx \pm 0.085$. This behaviour is not observed in aligned stacking, which preserves particle hole symmetry. In aligned stacking the OMMs coincide. Here the system shows a different behaviour in different cyclic stacking than in aligned stacking, which is an unusual behaviour. For intermediate values ($0 < \alpha < 1$) the time-reversal, inversion and particle-hole symmetries are broken. This leads to a fundamental difference compared to aligned stacks. In OMMs, each individual band is assigned a different value. This system is characterised by exotic topological properties, as confirmed by the introduction of the Haldane term to describe topological insulating systems[55].

Following the analogy of aligned systems, we explore the topological characteristics of OMMs by examining the variation of $m(k = 0)$ with α for the two valleys illustrated in Fig.7(ii)-(iii). For the K valley, the OMMs associated with the wavy bands $\varepsilon_2(k)$ and $\varepsilon_5(k)$, as well as the conduction band $\varepsilon_6(k)$ and the valence band $\varepsilon_3(k)$, exhibit a

sign change. Intriguingly, we observe that the OMM transitions from a negative sign throughout the α range until it reaches $1/\sqrt{2}$, where it becomes positive. This behavior stands in contrast to that observed in aligned stacks. In contrast, the conduction band $\varepsilon_6(k)$ and the valence band $\varepsilon_3(k)$ exhibit a monotonic dependence on α . For the K' valley, the roles of the conduction band $\varepsilon_4(k)$ and the valence band $\varepsilon_1(k)$ are reversed with those of the conduction band $\varepsilon_6(k)$ and the valence band $\varepsilon_3(k)$, respectively. The wavy band $\varepsilon_2(k)$ also exchanges its role with the wavy band $\varepsilon_5(k)$.

D. Orbital Magnetization

Orbital magnetization is a fascinating property of crystalline materials where time-reversal symmetry is broken. Often referred to as the "modern theory of orbital magnetization," this understanding is based on developments in the Berry phase theory of orbital magnetization [70, 73, 74]. An illustrative derivation of orbital magnetization is presented, based on the semiclassical approach to the dynamics of wave packets for Bloch electrons[74], the Wannier function approach[73, 75], or perturbation theory[70]. These methods address two closely related quantities: the orbital moment magnetization (OMM) and the Berry curvature (To understand how this phenomenon evolved from its initial inception to its modern development, I recommend the reader to refer to this review by T. Thonhauser[76]). Orbital magnetization is a thermodynamic quantity that can be derived from the differentiation of the grand canonical potential with respect to the magnetic field. This grand canonical potential, which represents the free energy of a free particle in the presence of a weak magnetic field \mathbf{B} , can be written as follows:

$$F^\xi = -\frac{1}{\beta} \sum_{k,m} \ln \left(1 + e^{-\beta(E_m^\xi(\mathbf{k}) - \mu)} \right) \quad (31)$$

In the presence of a weak magnetic field \mathbf{B} , the electronic energy $E_m^\xi(\mathbf{k}) = \varepsilon_m^\xi(\mathbf{k}) - \mathbf{m}(\mathbf{k}) \cdot \mathbf{B}$ acquires a correction term due to the orbital magnetic moment $\mathbf{m}(\mathbf{k})$ [69, 77]. Additionally, the parameter $\beta = 1/(k_B T)$, where k_B is the Boltzmann constant, T is the temperature, and μ is the chemical potential.

Building on a semi-classical approach, Xiao et al.[72] rigorously showed that the Berry curvature affects the distribution of states within phase space. In the presence of a weak external magnetic field \mathbf{B} , the summation over k can be transformed into an integral expressed as $\sum_k \rightarrow \frac{1}{(2\pi)^2} \int^\mu \left(1 + \frac{e\mathbf{B} \cdot \boldsymbol{\Omega}^m(\mathbf{k})}{\hbar} \right) d\mathbf{k}$. This transformation arises from the violation of Liouville's theorem due to the non-conservation of phase space volume.

The magnetization is then the derivative of the free energy of the magnetic field \mathbf{B} at fixed T and μ : $\mathbf{M} = -(\partial F / \partial \mathbf{B})_{\mu, T}$, which leads to

$$\mathbf{M}(\mathbf{r}) = \frac{1}{(2\pi)^2} \sum_m \int d\mathbf{k} f(\mathbf{k}) \mathbf{m}(\mathbf{k}) + \frac{e}{2\pi\beta\hbar} \sum_m \int d\mathbf{k} \boldsymbol{\Omega}^m(\mathbf{k}) \log \left(1 + e^{-\beta(\varepsilon - \mu)} \right) \quad (32)$$

This expression for magnetization is derived under equilibrium conditions, specifically for zero external magnetic field but applicable to a broad range of temperatures. The term $f(\mathbf{k}) = (1 + e^{\beta(\varepsilon(\mathbf{k}) - \mu)})^{-1}$ represents the Fermi-Dirac distribution function. The integration in equation (32) exhibits two different contributions: the first term originates from the self-rotation of the wave packet, and the second term is due to the motion of the wave packet's center of mass.

To gain insights into the behavior of $M(\mathbf{r})$ in the two scenarios of irradiated lattices for aligned stacking and cyclic stacking, we numerically evaluated the integrals \mathbf{k} in equations (32). To delve into the impact of chemical potential μ on the system, we plotted the curves for distinct values of α ($\alpha = 0, 0.4$, and 0.8) at a constant temperature of $T = 100$ K, as illustrated in Figures 8(i) and 8(ii). The interactions between matter and photons are modulated by the light-induced mass term Δ . We consider two values of Δ , namely $\Delta = 50$ meV and $\Delta = 100$ meV.

In aligned lattices, magnetization exhibits a significant increase with increasing Δ for all values of α . It displays an antisymmetric function for $\alpha = 0$ and $\alpha = 1$ and changes sign with the change of sign of μ . Furthermore, it transitions from a negative (positive) value to a positive (negative) value around $\mu = 0$. Notably, the antisymmetry of magnetization vanishes for $\alpha = 0.4$ and $\alpha = 0.8$, indicating its absence in these specific cases. This disappearance can be attributed to the breaking of the hole-particle symmetry. Topological signatures of orbital magnetization can be visualized by examining its dependence on μ in $\Delta = 50$ meV. For $\alpha = 0$, the magnetization exhibits a linear variation with μ , indicating that the interval of μ in which magnetization is linear is limited by the energy gap between the conduction bands (or valence bands). In the case of $\alpha \neq 1$, the magnetization varies linearly with μ when the interval of μ corresponds to the energy gap between the conduction band and the flat band (or between the valence band and the flat band). This linear variation of magnetization with μ in this energy gap constitutes a topological signature,

as mentioned by Ceresoli[71], and reveals a relationship between magnetization and the Chern number, expressed by $dM/d\mu = e/h \sum_m^{occ} C_m$. In cyclic lattices, magnetization exhibits a significant increase with the rise in Δ for $\alpha = 0$ and $\alpha = 1$. However, for $\alpha = 0.4$ and $\alpha = 0.8$, the magnetization does not follow the same growth pattern. When $\alpha = 0$, the magnetization changes in an antisymmetric manner with respect to μ , while for $\alpha = 1$, it changes symmetrically. This distinct behavior contrasts with the aligned system where $\alpha = 1$. The symmetric and antisymmetric nature disappears for $\alpha = 0.4$ and $\alpha = 0.8$, due to the breaking of particle-hole symmetry. As previously mentioned, in the aligned system, the topological characteristics in this cyclic system cause the magnetization to vary linearly with μ , indicating that the μ interval within which the magnetization remains linear is limited by the gap energy.

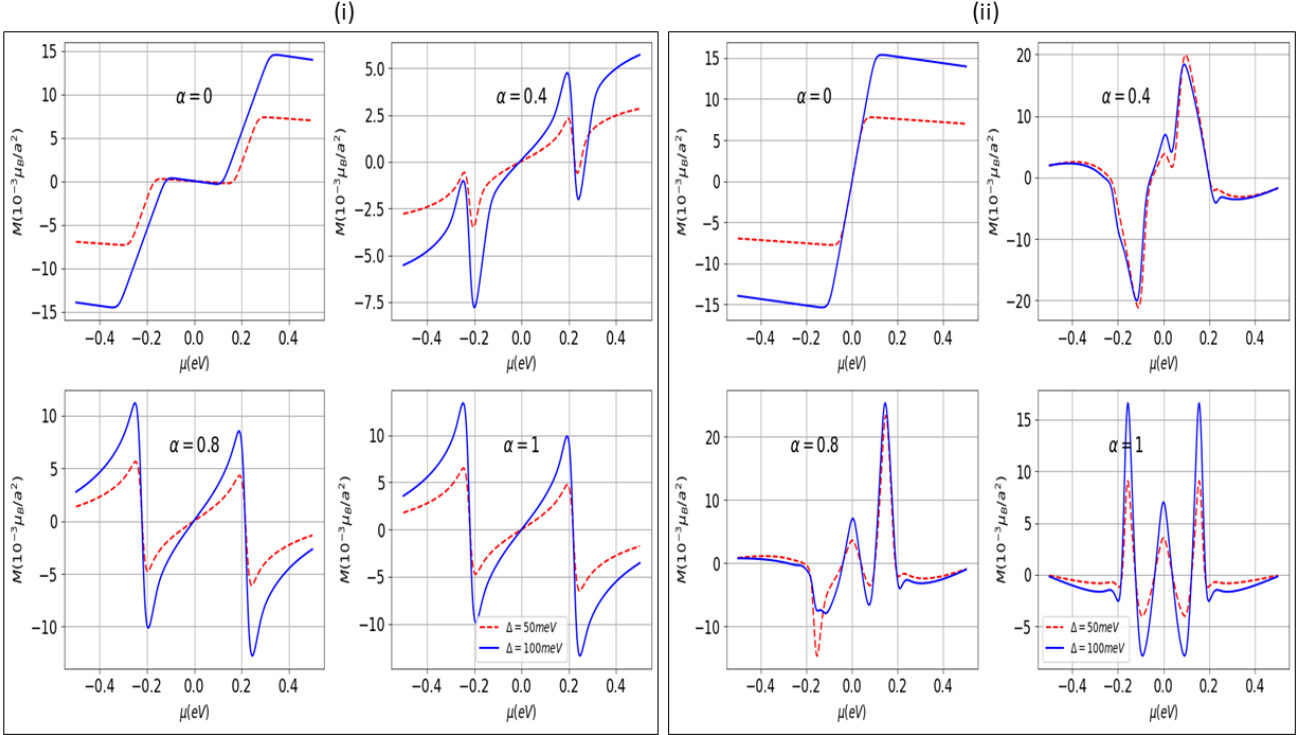


FIG. 8. Orbital magnetism in an $\alpha - T_3$ bilayer in an aligned stack (i) and a cyclic stack (ii) at valley K: dependence as a function of chemical potential μ for different values of α . The temperature considered is $T = 100$ K.

We investigate the evolution of magnetization M in aligned and cyclic stacking lattices as a function of chemical potential μ , considering both the K and K' valleys with $\Delta = 50$ meV and $T = 100$ K, as illustrated in Figures 9(i) and 9(ii). The results show that, due to particle-hole symmetry, the magnetization in the K and K' valleys coincides for $\alpha = 0$ and $\alpha = 1$. However, for $0 < \alpha < 1$, the magnetization in the two valleys exhibits a pronounced difference, attributed to the breaking of particle-hole and time-reversal symmetries

E. Thermal Hall conductivity

This section explores the interesting field of the Anomalous Hall Effect (AHE) in irradiated, aligned and cyclic $\alpha - T_3$ bilayer lattices. The AHE has captivated researchers with its counterintuitive nature: the spontaneous appearance of a significant Hall current in a ferromagnetic material when exposed to an applied electric field alone, defying the conventional requirement of an external magnetic field [78]. The intricate microscopic mechanisms governing AHE remain a subject of ongoing debate within the scientific community, despite its longstanding presence (over a century) and critical role in material characterisation [79].

Three main mechanisms historically proposed to contribute to AHE are the intrinsic contribution, and extrinsic contributions from obliquity and side jump scattering [80–83]. Specifically, the intrinsic contribution, which is independent of scattering processes, is attributed to the anomalous velocity induced by the Berry phase, a geometric

property characterizing the electronic band structure. This intrinsic contribution can be conceptualized as an unquantized counterpart to the well-established quantum Hall effect. Interestingly, some earlier work suggests a particularly remarkable scenario: Berry curvature alone determines anomalous Hall conductivity (AHC)[84].

$$\sigma_{xy}^{\xi} = \frac{e^2}{h} \sum_m \int \frac{d^2k}{(2\pi)^2} \Omega_m^{\xi}(\mathbf{k}) f_m^{\xi}(\mathbf{k}) \quad (33)$$

To elucidate the intrinsic contribution to the AHE, we leverage a generic effective Hamiltonian (16) that captures the electronic properties within the aligned and cyclically irradiated bilayer network. Notably, the electronic bands exhibit band crossings at points denoted as t^a (t^c). A mass term, induced by a circular vector potential, separates these bands. Subsequently, the AHC, σ_{xy} , is calculated numerically using Eq (33). Figures 10(i) and 10(ii) depict the evolution of the AHC as a function of the chemical potential for the aligned and cyclic systems, respectively. These calculations are conducted at a fixed temperature of $T = 50$ K, with an irradiation strength of $\Delta = 50$ meV for the aligned stacking and $\Delta = 100$ meV for the cyclic stacking.

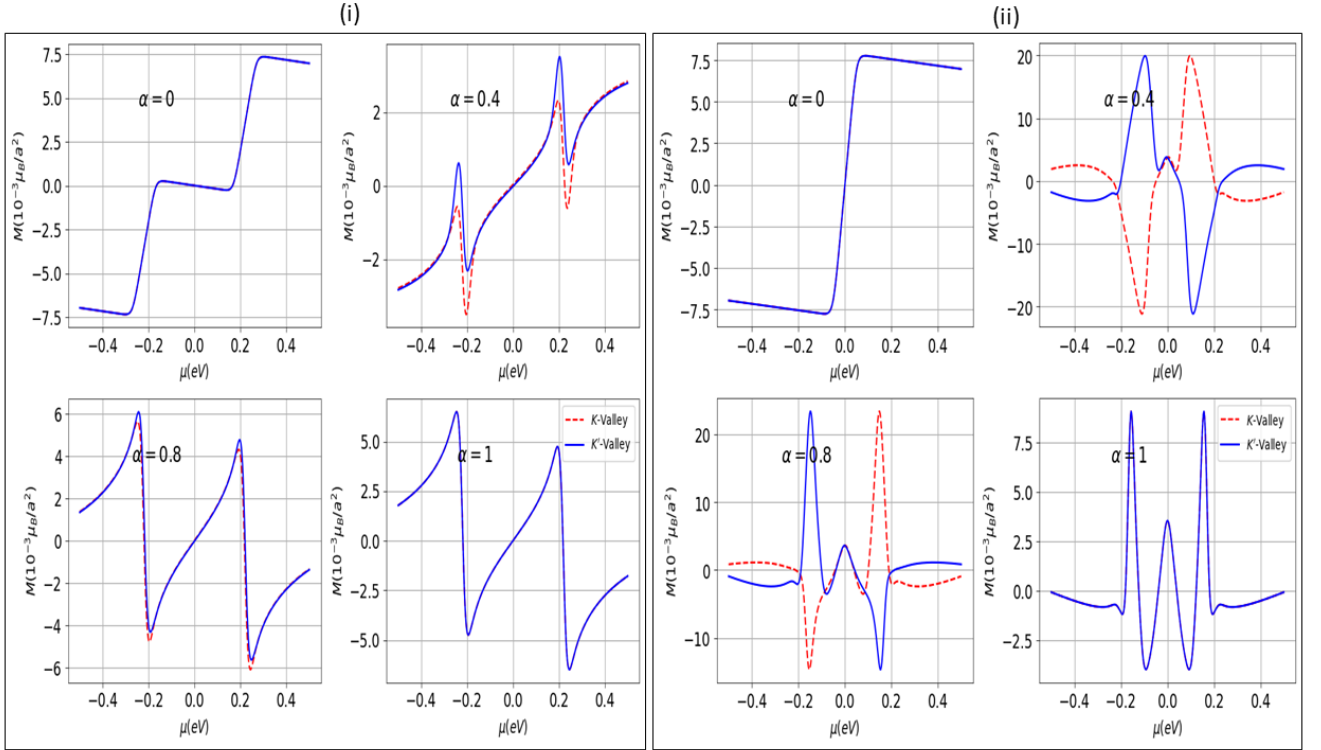


FIG. 9. Distribution of Orbital Magnetization in an aligned stack (i) and a cyclic stack (ii) as a function of chemical potential μ for valleys K and K', with $\Delta = 50$ meV and $T = 100k$.

To investigate the intrinsic contribution to the AHC within aligned $\alpha - T_3$ bilayer lattices, we first examine the AHC for both valleys. As shown in Figure 10(i), the AHC for both valleys can be represented as a superposition of two AHC blocks originating from the single layer $\alpha - T_3$ systems. These blocks are shifted relative to each other as the chemical potential μ approaches the flat energy region (equivalently, the interlayer coupling energy, t^a) and deviates from zero. When μ is in the gap region Δ , where AHC reaches its maximum values and approaches $\frac{1}{2}e^2/h$ ($\alpha = 0$) and e^2/h ($\alpha = 1$), the states with occupied energy just below Δ contribute most to the Hall conductivity σ_{xy} . For μ values above Δ , the contributions from the upper and lower bands cancel each other out, leading to a decrease in AHC as μ moves further away from the gap Δ . This behaviour highlights the significant enhancement in conductivity when μ is confined within the gap region Δ . The flat bands themselves do not contribute to the Hall conductivity. Since the corresponding Berry curvature vanishes, the flat bands themselves do not contribute to σ_{xy} . Furthermore, it is observed that the σ_{xy} for $\alpha = 1$ is double that for $\alpha = 0$. Since the particle-hole symmetry is preserved, the conductivities for both valleys coincide at $\alpha = 0$ and $\alpha = 1$. In contrast to the behavior observed at $\alpha = 0$ and $\alpha = 1$, where particle-hole symmetry holds, the scenario for $\alpha \neq 0, 1$ reveals distinct characteristics. Here, we witness the

emergence of valleys exhibiting contrasting behavior in the σ_{xy} . This observation signifies a breakdown of particle-hole symmetry within the system. Similar to the cases of $\alpha = 0$ and $\alpha = 1$, two distinct AHC blocks emerge at $\mu = t^a$ and $\mu = -t^a$. Focusing on the block where μ is near t^a , a unique two-plateau structure becomes evident, arising from the presence of two band gaps of unequal sizes. As μ approaches $t^a - \Delta$, the plateau associated with valley K' comes into focus. Conversely, when μ approaches $t^a + \Delta$, the plateau corresponding to valley K dominates. The total AHC, which represents the combined contributions from both valleys, exhibits a notable behavior. It approaches the quantized values of e^2/h and $2e^2/h$ within the band gaps $t-d$ and $t^a + \Delta$, when α falls below ($\alpha < 1/\sqrt{2}$) and exceeds ($\alpha > 1/\sqrt{2}$) the value of $1/\sqrt{2}$. This observation provides strong evidence for a topological phase transition occurring at a critical value of $\alpha = 1/\sqrt{2}$.

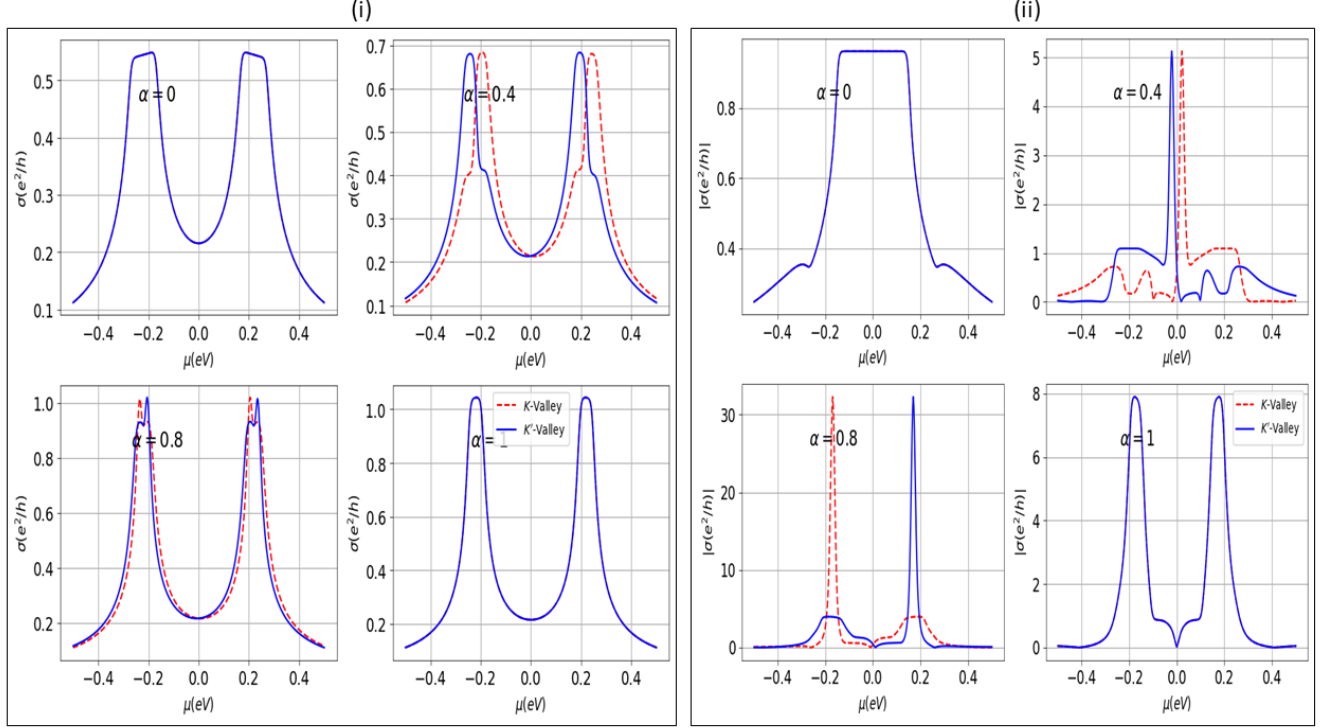


FIG. 10. Anomalous Hall conductivity of the aligned stack (i), with $\Delta = 50\text{meV}$, and the cyclic stack (ii), with $\Delta = 100\text{meV}$, as a function of chemical potential, for various values of α , calculated in both K and K' valleys, at temperature $T = 50k$.

This analysis explores the anomalous Hall conductivity of the cyclically stacked α - T_3 bilayer as a function of the chemical potential μ , as illustrated in Figure 10(ii). It is observed that the Hall conductivity σ_{xy} for both valleys is identical, reflecting the conservation of particle-hole symmetry for $\alpha = 0$ and $\alpha = 1$. Within the bandgap, variations in the chemical potential result in the formation of a plateau in σ_{xy} , with a width proportional to Δ , which arises from the contributions of all occupied states in the valence band. In contrast to the aligned configuration, the corrugated band provides an additional contribution to σ_{xy} due to its non-vanishing Berry curvature. In $\alpha - T_3$ bilayers with $\alpha \neq 0$ and $\alpha \neq 1$, the breakdown of particle-hole symmetry gives rise to valley-dependent behaviour in σ_{xy} , which is distinct from the behaviour observed in bilayers with other values of α . The presence of two unequal forbidden bands in the quasi-energy spectrum for each valley results in a two-plateau structure near the bandgap edge ($\mu \approx t^c$ and $\mu \approx -t^c$). These properties are more pronounced at decreased temperatures and elevated Δ values, although they are not included in this analysis. The total AHC, σ_{xy} , is the sum of contributions from the K and K' valleys. As illustrated in Figure 10(ii), within the band gaps of these valleys, the AHC approaches a quantized value of $1e^2/h$ for $\alpha < 1/\sqrt{2}$, $4e^2/h$ for $\alpha = 0.4$, and $16e^2/h$ for $\alpha = 1$. The exceptionally high AHC observed for $\alpha = 0.8$ and $\alpha = 1$ confirms a topological phase transition at $\alpha = 1/\sqrt{2}$.

In the off-resonance irradiated cyclic stack and effective control of external parameters, notably the amplitude of the light field, proportional to Δ . In this context, we find σ_{xy} plateaus appearing for values of $\alpha = 0.4$ and 0.8 . The responses of the two valleys, K and K', show values close to $1e^2/h$ and $4e^2/h$, similar to those obtained in the Haldane model applied to a cyclic stack, as discussed in P.Parui[55]. Thus, Floquet Engineering presents a programmable solution to realize the Haldane model and control topological phases.

III. CONCLUSION

In this study, we investigated the topological signatures induced by circularly polarized light on $\alpha - T_3$ bilayer networks. The bilayer $\alpha - T_3$ lattice we examined exhibited two distinct commensurate stacking configurations: AA-BB-CC alignment and AB-BC-CA cyclic. Our effective model accurately captured the topological features associated with the K and K' band crossing points. As we have seen, circular off-resonance polarization breaking time reversal symmetry induces a Haldane-type Chern insulator in the $\alpha - T_3$ bilayer when the phase $\varphi = \pi/2$ and $\Delta^\xi = -t_2 3\sqrt{3}$ are fixed at the Dirac point[55]. This makes it possible to realize a Haldane insulator by controlling the system parameters and the polarization amplitude. By analyzing the discrete symmetries of the system, we identified a broken time-reversal symmetry at $\alpha = 0$ and a broken particle-hole symmetry at $\alpha = 1$. These stacking configurations exhibit distinct energy spectra. By analyzing various Berry phase effects, we identified topological signatures in both the aligned and cyclic $\alpha - T_3$ lattices. Our calculations of Berry curvature, orbital magnetic moment, orbital magnetization, and anomalous Hall conductivity revealed the topological nature of these quantities. Notably, a critical transition occurs at $\alpha = 1/\sqrt{2}$, where the Berry curvature and orbital magnetic moment associated with the flat band in aligned stacks and the corrugated band in cyclic stacks undergo a significant change. The light-driven effect on the flat and corrugated bands near the Dirac points results primarily in two distinct, α -dependent, equal-width bandgaps at the t^a/t^c intersections. Within these bandgaps the orbital magnetization shows a linear dependence on the chemical potential. The gradient of this linear relationship is steeper for $\alpha = 0.4$ compared to $\alpha = 0.8$. Around $\alpha = 1/\sqrt{2}$ this difference in steepness is strongly correlated with the Chern number transition. As the chemical potential falls into the band gap, the anomalous Hall conductivity takes on quantized values, i.e. a plateau. For $0 < \alpha < 1$, for aligned stacking and cyclic stacking, a 'two plateau' structure is observed in the Hall conductivity of the K and K' valleys. Nevertheless, the total anomalous conductivity of the individual valleys k and k' with respect to aligned stacking in band gaps when the chemical potentials are $t^a + \Delta$ and $t^a - \Delta$ or $-t^a - \Delta$ and $-t^a + \Delta$ approaches e^2/h and $2e^2/h$ respectively, approximately when $\alpha < 1/\sqrt{2}$ and $\alpha > 1/\sqrt{2}$, respectively, in cyclic stacking the AHC approaches a quantum value of $1e^2/h$ for $\alpha < 1/\sqrt{2}$, $4e^2/h$ for $\alpha = 0.4$ and $16e^2/h$ for $\alpha = 1$. As we observe plateaus at $\alpha = 0.4$ and 0.8 in the K and K' valleys, these correspond to the plateaus in the Haldane model for cyclic stacking. In both stacks, for $0 < \alpha < 1$, broken particle-hole symmetry leads to distinct valley patterns in the orbital magnetisation and the AHC. By analyzing the results along with prior data for $\alpha = 1$, it is observed that the valley induced by the particle-hole symmetry and the inversion symmetries in alignment stacks, as well as the particle-hole symmetries in cyclic stacks, lead to the disappearance of the Berry curvature associated with the flat band. In contrast, the flat band is crucial in determining the orbital magnetic moment in the alignment stacks. However, in the cyclic stacks, the Berry curvature associated with the corrugated band becomes dominant at $k = 0$. This corrugated band significantly enhances the value of the orbital magnetic moment, which remains positive at $k = 0$. The $\alpha - T_3$ bilayer lattice may enable the development of highly sensitive quantum sensors that can detect subtle polarized radiation or magnetic fields by altering material properties in response to these fields. This lattice also has applications in optoelectronics, especially in secure communication systems that encode information via light polarization, and in valley-caloritronics. It presents new opportunities for quantum computers and fast, efficient electronic devices by controlling electron properties at the energy valley level, facilitating innovative information storage and processing methods.

ACKNOWLEDGMENT

The authors would like to acknowledge the "Académie Hassan II des Sciences et Techniques"-Morocco for its financial support. The authors also thank the LPHE-MS, Faculty of Sciences, Mohammed V University in Rabat, Morocco for the technical support through facilities.

-
- [1] Nagaosa, N., et Tokura, Y. (2013). Topological properties and dynamics of magnetic skyrmions. *Nature nanotechnology*, 8(12), 899-911.
 - [2] L. B. Drissi, E. H. Saidi, and M. Bousmina, Four-dimensional graphene. *Physical Review D*, 2011, vol. 84, no 1, p. 014504.
 - [3] C. C. Liu, W. Feng, Y. Yao, spin Hall effect in silicene and two-dimensional germanium. *Physical review letters*, 2011, vol. 107, no 7, p. 076802.
 - [4] L. B. Drissi, E. H. Saidi, Domain Walls in Topological Tri-hinge Matter, *European Physical Journal Plus* 136 (2021) 68.
 - [5] D. Hsieh, D. Qian, L. Wray, Y. Xia, Y. S. Hor, R. J. Cava, M. Z. Hasan, A topological Dirac insulator in a quantum spin Hall phase. *Nature* 452 (2008) 970-974.

- [6] R. Roy, Z_2 classification of quantum spin Hall systems: An approach using time-reversal invariance. *Phys. Rev. B* 79 (2009) 195321.
- [7] L. B. Drissi, E. H. Saidi, Dirac zero Modes in Hyperdiamond Model, *Phys. Rev. D* 84 (2011) 014509.
- [8] M. Z. Hasan, C. L. Kane, Colloquium: topological insulators, *Rev. Mod. Phys* 82 (2010) 3045.
- [9] M. Ragragui, L. B. Drissi, H. Saidi, Evidence of topological surface states in dysprosium monpnictides compounds, *Materials Science and Engineering: B* 283 (2022) 115774.
- [10] B. Q. Lv, et al., Experimental discovery of Weyl semimetal TaAs, *Phys. Rev. X* 5 (2015) 031013.
- [11] F. Schindler, A. M. Cook, M. G. Vergniory, Z. Wang, S. S. Parkin, B. A. Bernevig, and T. Neupert, Higher order topological insulators, *Science advances* 4 (2018) eaat0346.
- [12] Hiromu Araki, Tomonari Mizoguchi, Yasuhiro Hatsugai, ZQ Berry Phase for Higher-Order Symmetry-Protected Topological Phases, *Phys. Rev. Research* 2 (2020) 012009.
- [13] L. B. Drissi, S. Lounis, E. H. Saidi, Higher order topological matter and fractional chiral states, *The European Physical Journal Plus* 137, Article number: 796 (2022)
- [14] N. Bultinck, B. A. Bernevig, M. P. Zaletel, Three dimensional superconductors with hybrid higher-order topology, *Phys. Rev. B* 99 (2019) 125149.
- [15] Elbahri, A., Ragragui, M., Drissi, L.B., Saidi, E.H., Exploring topological phases in superconducting transition metal (Sc, Ti, V)-carbides, *Materials Science in Semiconductor Processing* 2025, 186, 108993.
- [16] M-S. Rudner & N-H. Lindner, Band structure engineering and non-equilibrium dynamics in Floquet topological insulators, *Nature Reviews Physics* volume 2, pages229–244 (2020).
- [17] J. Minguzzi, Z. Zhu, K. Sandholzer, AS. Walter, K. Viebahn, T. Esslinger, Topological pumping in a Floquet-Bloch band, *Physical Review Letters* 129 (5), 053201 (2022).
- [18] L. B. Drissi, E. H. Saidi, and M. Bousmina, Electronic properties and hidden symmetries of graphene. *Nuclear Physics B*, 2010, vol. 829, no 3, p. 523-533.
- [19] C. C. Liu, W. Feng, Y. Yao, spin Hall effect in silicene and two-dimensional germanium. *Physical review letters*, 2011, vol. 107, no 7, p. 076802.
- [20] M. Houssa, B. Broek, K. Iordanidou, A. Lu, G. Pourtois, J. P. Locquet, V. Afanas'ev, and A. Stesmans, Topological to trivial insulating phase transition in stanene. *Nano Research*, 2016, vol. 9, p. 774-778.
- [21] Delplace, P., Gomez-Leon, ., et Platero, G. (2013). Merging of Dirac points and Floquet topological transitions in ac-driven graphene. *Physical Review B- Condensed Matter and Materials Physics*, 88(24), 245422.
- [22] B. Bentaibi, L. B. Drissi, E. H. Saidi, M. Bousmina, New room-temperature 2D hexagonal topological insulator OsC: First Principle Calculations. *Materials Science in Semiconductor Processing*, 2022, vol. 151, p. 107009.
- [23] N. Goldman and J. Dalibard, Periodically Driven Quantum Systems: Effective Hamiltonians and Engineered Gauge Fields, *PHYSICAL REVIEW X* 4, 031027 (2014).
- [24] L.B. Drissi, J. Kanga, S. Lounis, F. Djeflal, S. Haddad, Electron-phonon dynamics in 2D carbon based-hybrids XC ($X = Si, Ge, Sn$). *Journal of Physics: Condensed Matter*, 2019, vol. 31, no 13, p. 135702.
- [25] Cao, Y., Fatemi, V., Fang, S., Watanabe, K., Taniguchi, T., Kaxiras, E., et Jarillo-Herrero, P. (2018). Unconventional superconductivity in magic-angle graphene superlattices. *Nature*, 556(7699), 43-50.
- [26] Chen, G., Jiang, L., Wu, S., Lyu, B., Li, H., Chittari, B. L., ... et Wang, F. (2019). Evidence of a gate-tunable Mott insulator in a trilayer graphene moiré superlattice. *Nature Physics*, 15(3), 237-241.
- [27] Sinha, S., Adak, P. C., Surya Kanthi, R. S., Chittari, B. L., Sangani, L. V., Watanabe, K., ... et Deshmukh, M. M. (2020). Bulk valley transport and Berry curvature spreading at the edge of flat bands. *Nature communications*, 11(1), 5548.
- [28] I. Serifi, N.B.-J. Kanga, L. B. Drissi, A. Kara, E.H. Saidi, Electron-Phonon Superconductivity in Boron-Based Chalcogenide ($X = S, Se$) Monolayers, *Annalen der Physik* 535, 5 (2023) 220053.
- [29] Oka, T., et Aoki, H. (2009). Photovoltaic Hall effect in graphene. *Physical Review B, condensed Matter and Materials Physics*, 79(8), 081406.
- [30] Lopez, A., Sun, Z. Z., et Schliemann, J. (2012). Floquet spin states in graphene under ac-driven spin-orbit interaction. *Physical Review B*, 85(20), 205428.
- [31] Agarwala, A., Bhattacharya, U., Dutta, A., et Sen, D. (2016). Effects of periodic kicking on dispersion and wave packet dynamics in graphene. *Physical Review B*, 93(17), 174301.
- [32] A. Bhattacharya and SK F. Islam, Photoinduced spin-Hall resonance in a k^3 -Rashba spin-orbit coupled two-dimensional hole system, *Phys. Rev. B* 104, L081411 (2021).
- [33] Guo, H. M., et Franz, M. (2009). Topological insulator on the kagome lattice. *Physical Review B*, 80(11), 113102.
- [34] Vidal, J., Mosseri, R., et Douçot, B. (1998). Aharonov-Bohm cages in two-dimensional structures. *Physical review letters*, 81(26), 5888.
- [35] Goldman, N., Urban, D. F., et Bercioux, D. (2011). Topological phases for fermionic cold atoms on the Lieb lattice. *Physical Review A—Atomic, Molecular, and Optical Physics*, 83(6), 063601.
- [36] Liu, H., Meng, S., et Liu, F. (2021). Screening two-dimensional materials with topological flat bands. *Physical Review Materials*, 5(8), 084203.
- [37] Rhim, J. W., et Yang, B. J. (2019). Classification of flat bands according to the band-crossing singularity of Bloch wave functions. *Physical Review B*, 99(4), 045107. [
- [38] Wang, F., et Ran, Y. (2011). Nearly flat band with Chern number $C = 2$ on the dice lattice. *Physical Review B*, 84(24), 241103.
- [39] Rizzi, M., Cataudella, V., et Fazio, R. (2006). Phase diagram of the Bose-Hubbard model with T_3 symmetry. *Physical Review B—Condensed Matter and Materials Physics*, 73(14), 144511.

- [40] Raoux, A., Morigi, M., Fuchs, J. N., Piéchon, F., et Montambaux, G. (2014). From dia-to paramagnetic orbital susceptibility of massless fermions. *Physical review letters*, 112(2), 026402.
- [41] Malcolm, J. D., et Nicol, E. J. (2015). Magneto-optics of massless Kane fermions: Role of the flat band and unusual Berry phase. *Physical Review B*, 92(3), 035118.
- [42] Biswas, T., et Ghosh, T. K. (2016). Magnetotransport properties of the $\alpha - T_3$ model. *Journal of Physics: Condensed Matter*, 28(49), 495302.
- [43] Benhaida, O., Hassan, S. E., et Drissi, L. B. (2025). Optically Controlled Topological Phases in the Deformed $\alpha - T_3$ Lattice. arXiv preprint arXiv:2503.22146.
- [44] Chen, Y. R., Xu, Y., Wang, J., Liu, J. F., et Ma, Z. (2019). Enhanced magneto-optical response due to the flat band in nanoribbons made from the $\alpha - T_3$ lattice. *Physical Review B*, 99(4), 045420.
- [45] Illes, E., Carbotte, J. P., et Nicol, E. J. (2015). Hall quantization and optical conductivity evolution with variable Berry phase in the $\alpha - T_3$ model. *Physical Review B*, 92(24), 245410.
- [46] Dey, B., et Ghosh, T. K. (2018). Photoinduced valley and electron-hole symmetry breaking in $\alpha - T_3$ lattice: The role of a variable Berry phase. *Physical Review B*, 98(7), 075422.
- [47] Dura, B., Cayssol, J., Simon, F., et Moessner, R. (2012). Optically engineering the topological properties of a spin Hall insulator. *Physical review letters*, 108(5), 056602.
- [48] Ezawa, M. (2013). Photoinduced topological phase transition and a single Dirac-cone state in silicene. *Physical review letters*, 110(2), 026603.
- [49] Saha, K. (2016). Photoinduced Chern insulating states in semi-Dirac materials. *Physical Review B*, 94(8), 081103.
- [50] Tahir, M., Manchon, A., et Schwingenschlögl, U. (2014). Photoinduced quantum spin and valley Hall effects, and orbital magnetization in monolayer MoS_2 . *Physical Review B*, 90(12), 125438.
- [51] Dey, B., Kapri, P., Pal, O., et Ghosh, T. K. (2020). Unconventional phases in a Haldane model of dice lattice. *Physical Review B*, 101(23), 235406.
- [52] Wang, F., et Ran, Y. (2011). Nearly flat band with Chern number $C = 2$ on the dice lattice. *Physical Review B- Condensed Matter and Materials Physics*, 84(24), 241103.
- [53] Tamang, L., et Biswas, T. (2023). Probing topological signatures in an optically driven $\alpha - T_3$ lattice. *Physical Review B*, 107(8), 085408.
- [54] Sukhachov, P. O., Oriekhov, D. O., et Gorbar, E. V. (2023). Stackings and effective models of bilayer dice lattices. *Physical Review B*, 108(7), 075166.
- [55] Parui, P., Ghosh, S., et Chittari, B. L. (2024). Topological properties of nearly flat bands in bilayer $\alpha - T_3$ lattice. *Physical Review B*, 109(16), 165118.
- [56] Niu, Z. P., et Wang, S. J. (2022). Valley polarized transport and negative differential resistance in an irradiated lattice. *Journal of Physics D: Applied Physics*, 55(25), 255303.
- [57] Sukhachov, P. O., Oriekhov, D. O., et Gorbar, E. V. (2023). Stackings and effective models of bilayer dice lattices. *Physical Review B*, 108(7), 075166.
- [58] Benhaida, O., Drissi, L. B., Saidi, E. H., et Laamara, R. A. (2024). Klein tunneling and Fabry-Perot resonances in the $\alpha - T_3$ bilayer with aligned stacking. *Physica Scripta*, 99(8), 085958.
- [59] Rodriguez-Vega, Martin, Vogl, Michael, et Fiete, Gregory A. Moiré-Floquet engineering of quantum materials: a review. arXiv e-prints, 2020, p. arXiv: 2011.11079.
- [60] Platero, G., et Aguado, R. (2004). Photon-assisted transport in semiconductor nanostructures. *Physics Reports*, 395(1-2), 1-157.
- [61] Busl, M., Platero, G., et Jauho, A. P. (2012). Dynamical polarizability of graphene irradiated by circularly polarized ac electric fields. *Physical Review B*, 85(15), 155449.
- [62] Zou, J. Y., et Liu, B. G. (2016). Floquet Weyl fermions in three-dimensional stacked graphene systems irradiated by circularly polarized light. *Physical Review B*, 93(20), 205435.
- [63] Huamán, A., et Usaj, G. (2019). Anomalous Goos-Hanchen shift in the Floquet scattering of Dirac fermions. *Physical Review A*, 100(3), 033409.
- [64] H. Sambe, Steady states and quasienergies of a quantum mechanical system in an oscillating field, *Phys. Rev. A* 7, 2203 (1973).
- [65] Dey, B., et Ghosh, T. K. (2019). Floquet topological phase transition in the $\alpha - T_3$ lattice. *Physical Review B*, 99(20), 205429..
- [66] Parui, P., Ghosh, S., et Chittari, B. L. (2024). Topological properties of nearly flat bands in bilayer $\alpha - T_3$ lattice. *Physical Review B*, 109(16), 165118.
- [67] Xiao, D., Chang, M. C., et Niu, Q. (2010). Berry phase effects on electronic properties. *Reviews of modern physics*, 82(3), 1959.
- [68] Souza, I., et Vanderbilt, D. (2008). Dichroic f-sum rule and the orbital magnetization of crystals. *Physical Review B*, 77(5), 054438
- [69] Chang, M. C., et Niu, Q. (1996). Berry phase, hyperorbits, and the Hofstadter spectrum: Semiclassical dynamics in magnetic Bloch bands. *Physical Review B*, 53(11), 7010.
- [70] Shi, J., Vignale, G., Xiao, D., et Niu, Q. (2007). Quantum theory of orbital magnetization and its generalization to interacting systems. *Physical review letters*, 99(19), 197202.
- [71] Ceresoli, D., Thonhauser, T., Vanderbilt, D., et Resta, R. (2006). Orbital magnetization in crystalline solids: Multi-band insulators, Chern insulators, and metals. *Physical Review B—Condensed Matter and Materials Physics*, 74(2), 024408.

- [72] Xiao, D., Shi, J., et Niu, Q. (2005). Berry phase correction to electron density of states in solids. *Physical review letters*, 95(13), 137204.
- [73] Thonhauser, T., Ceresoli, D., Vanderbilt, D., et Resta, R. (2005). Orbital magnetization in periodic insulators. *Physical review letters*, 95(13), 137205.
- [74] Xiao, D., Shi, J., et Niu, Q. (2005). Berry phase correction to electron density of states in solids. *Physical review letters*, 95(13), 137204.
- [75] Ceresoli, D., Thonhauser, T., Vanderbilt, D., et Resta, R. (2006). Orbital magnetization in crystalline solids: Multi-band insulators, Chern insulators, and metals. *Physical Review B—Condensed Matter and Materials Physics*, 74(2), 024408.
- [76] Thonhauser, T. (2011). Theory of orbital magnetization in solids. *International Journal of Modern Physics B*, 25(11), 1429-1458.
- [77] Sundaram, G., et Niu, Q. (1999). Wave-packet dynamics in slowly perturbed crystals: Gradient corrections and Berry-phase effects. *Physical Review B*, 59(23), 14915.
- [78] Chien, C. (Ed.). (2013). *The Hall effect and its applications*. Springer Science et Business Media.
- [79] Sinova, J., Culcer, D., Niu, Q., Sinitsyn, N. A., Jungwirth, T., et MacDonald, A. H. (2004). Universal intrinsic spin Hall effect. *Physical review letters*, 92(12), 126603.
- [80] Karplus, R., et Luttinger, J. M. (1954). Hall effect in ferromagnetics. *Physical Review*, 95(5), 1154.
- [81] Luttinger, J. M. (1958). Theory of the Hall effect in ferromagnetic substances. *Physical Review*, 112(3), 739.
- [82] Smit, J. (1958). The spontaneous Hall effect in ferromagnetics II. *Physica*, 24(1-5), 39-51.
- [83] Berger, L. (1970). Side-jump mechanism for the Hall effect of ferromagnets. *Physical Review B*, 2(11), 4559.
- [84] Jungwirth, T., Niu, Q., et MacDonald, A. H. (2002). Anomalous Hall effect in ferromagnetic semiconductors. *Physical review letters*, 88(20), 207208.
- [85] Lin, C. Y., Huang, B. L., Ho, C. H., Gumbs, G., et Lin, M. F. (2018). Geometry-diversified Coulomb excitations in trilayer AAB stacking graphene. *Physical Review B*, 98(19), 195442.